Energy Conversion and Management: X 28 (2025) 101253

Contents lists available at ScienceDirect

Energy Conversion and Management: X

journal homepage: www.sciencedirect.com/journal/energy-conversion-and-management-x

Numerical prediction of solar radiation in South Korea: assessment of WRF-Solar and WRF

Ji Won Yoon [a,b], Hyunsu Kim [c], Hae Soo Jung [d], Seon Ki Park [a,b,e,*]

[a] Center for Climate/Environment Change Prediction Research, Ewha Womans University, Seoul 03760, South Korea
[b] Severe Storm Research Center, Ewha Womans University, Seoul 03760, South Korea
[c] Central Load Dispatch Center, Korea Power Exchange, Naju-si, Jeollanam-do 58217, South Korea
[d] Korean Meteorological Society, Seoul 04195, South Korea
[e] Department of Climate and Energy Systems Engineering, Ewha Womans University, Seoul 03760, South Korea

ARTICLE INFO

Keywords:
WRF
WRF-Solar
Global Horizontal Irradiance
South Korea

ABSTRACT

This study aims to comparatively evaluate the performance of the Weather Research and Forecasting (WRF) model and the WRF-Solar model for forecasting global horizontal irradiance (GHI), a key factor in photovoltaic (PV) power generation, over South Korea during summer 2023. Experiments were conducted using WRF (CNTL) and WRF-Solar (EXP_R and EXP_F): All experiments used the same physical parameterization schemes, except for those specialized in WRF-Solar—Thompson–Eidhammer microphysics and Deng shallow cumulus (used in EXP_R and EXP_F), and Fast All-sky Radiation Model for Solar applications (FARMS) schemes (used only in EXP_F).

The GHI forecasts were evaluated across all (ALL), clear (CLR), cloudy (CLD), and overcast (OVC) sky conditions using in-situ and remote sensing data. Both EXP_R and EXP_F outperformed CNTL, with RMSE improvement of 7.2 – 19.9 % for EXP_R and 6.8 – 37.0 % for EXP_F. All experiments performed similarly under CLR; however, EXP_F outperformed EXP_R in other conditions, achieving up to 37.0 % improvement under OVC. The spatial distribution analysis also indicated improvements in WRF-Solar experiments, with EXP_F outperforming EXP_R. Additionally, WRF-Solar showed better cloud detection performance than WRF. In conclusion, this study demonstrates the first successful application of WRF-Solar in South Korea and highlights its potential to enhance energy management and solar power planning.

1. Introduction

Global warming due to anthropogenic greenhouse gases emitted from fossil fuels can cause climate change, triggering extreme weather events that severely impact ecosystems and human societies [1]. To address these issues, the global transition from fossil fuels to renewable energy is accelerating [2]. In response, South Korea declared 2050 Carbon Neutrality [3] and established the Renewable Energy 3020 Plan [4], aiming to generate 20 % of total electricity in the country from renewable sources by 2030. Specifically, solar energy was the primary contributor to electricity growth in 2023, generating more than twice the new electricity of coal and continuing as the fastest-growing power source for 19 years in a row [5].

Given that the global horizontal irradiance (GHI) is a key meteorological variable directly influencing photovoltaic (PV) systems [6], accurate GHI forecasting is essential for the stability of PV power generation. However, solar radiation is influenced not only by seasonal changes but also by weather conditions such as clouds, aerosols, and humidity, which introduce significant variability.

In South Korea, four distinct seasons—spring, summer, fall, and winter—result in significant seasonal variations in GHI. Among them, summer (June – August) experiences the highest solar radiation; however, the monsoon period from late June to mid-July brings increased cloud cover and precipitation, causing substantial fluctuations in GHI. Additionally, electricity demand peaks during this season due to cooling needs, further emphasizing the necessity of accurate GHI forecasting for the stable operation of PV power generation.

Although these challenges are especially noticeable in South Korea, similar issues in solar radiation forecasting are encountered in many regions worldwide. Therefore, various approaches have been employed to improve solar radiation forecasting, including statistical techniques, data-driven methods using machine learning (ML) and deep learning

* Corresponding author at: Center for Climate/Environment Change Prediction Research, Ewha Womans University, Seoul 03760, South Korea.
E-mail address: spark@ewha.ac.kr (S.K. Park).

https://doi.org/10.1016/j.ecmx.2025.101253
Received 4 March 2025; Received in revised form 1 June 2025; Accepted 5 September 2025
Available online 10 September 2025
2590-1745/© 2025 The Author(s). Published by Elsevier Ltd. This is an open access article under the CC BY-NC-ND license (http://creativecommons.org/licenses/by-nc-nd/4.0/).

(DL) algorithms, and numerical weather prediction (NWP) models. In particular, ML and DL techniques have been widely studied for solar irradiance forecasting, as they can effectively learn complex and nonlinear relationships between solar radiation and dynamic atmospheric variables—such as clouds, aerosols, humidity, and temperature—without relying on physical parameterizations: ML methods have demonstrated improved accuracy in short-term solar irradiance forecasting [7,8], particularly hybrid approaches—those combining ensemble feature selection or metaheuristic optimization techniques [9,10]. Similarly, DL methods have effectively captured spatiotemporal patterns in solar irradiance data, demonstrating improved performance across forecasts ranging from sub-hour to short-term [11–13]. More recently, data-driven models have shown notable performance in long-term solar radiation forecasting, outperforming traditional statistical methods [14,15]. However, the performance of ML and DL models is highly dependent on the quality and quantity of training data and tends to degrade under changing atmospheric conditions. These limitations become particularly pronounced under previously unobserved or data-sparse conditions, often resulting in reduced accuracy relative to physics-based models [16–18]. These limitations tend to become more evident in long-term forecasting.

Given these limitations, NWP models offer several key advantages in solar radiation forecasting, including the following: (1) NWP models effectively capture various weather elements closely related to solar radiation, including clouds, aerosols, and convection, by using complex atmospheric physics and dynamics. Moreover, simulating interactions between cloud microphysics and aerosols allows for more precise representation of weather conditions, thereby enhancing the accuracy of solar radiation forecasting [19]; (2) NWP models are effective not only in short-term but also in medium- to long-term forecasting, typically over 6 h [20], whereas data-driven approaches are more suitable for short-term forecasting [21]. This difference arises because the former predicts atmospheric flows, cloud formation, and the resulting changes in solar radiation based on atmospheric dynamics and physical equations, whereas the latter primarily relies on historical data to learn patterns and predict outcomes; (3) NWP models, applied with various temporal and spatial resolutions, allow more detailed solar radiation forecasting across different regions [22]. This flexibility enables accurate forecasts suited for specific locations and timeframes, contributing to the optimization of solar power generation and regional energy management strategies; (4) NWP models can predict not only solar radiation but also other weather variables such as temperature, humidity, and wind speed. Given that solar power depends on interrelated weather factors, NWP models can respond effectively to complex weather variations, thereby enabling more accurate predictions of solar power generation variability. Therefore, various global and regional NWP models are being utilized for solar radiation forecasting—e.g., Weather Research and Forecasting (WRF) [23], Regional Atmospheric Modeling System (RAMS) [24], COnsortium for Small-scale Modeling (COSMO) [25], Global Forecast System (GFS) [26], North American Mesoscale (NAM) [27], etc.

Recently, WRF-Solar, an enhanced version of WRF, was developed to meet the increasing need for specialized numerical forecast products for solar power applications [19]. It improves the accuracy of solar irradiance forecasting by incorporating enhanced cloud-aerosol-radiation feedback, efficient radiation parameterization, and improved subgrid-scale cloud representation [19,28,29].

As the importance of solar energy continues to rise, WRF-Solar has been widely employed in various studies: Jiménez et al. [30] demonstrated that increasing the resolution and activating the radiative effects of unresolved clouds in WRF-Solar improve forecast accuracy; Sawadogo et al. [31] showed that WRF-Solar performs reliably overall, with enhanced accuracy under clear-sky conditions relative to cloudy-sky conditions; Thaker and Höller [32] assessed high-resolution WRF-Solar using ground observations and found it outperformed both the low-resolution WRF-Solar and the Global Forecast System (GFS); Yue et al. [33] showed that WRF-Solar effectively captured both the spatial and temporal variability of GHI; Khamees et al. [34] conducted sensitivity experiments using various shortwave radiation schemes in WRF-Solar, showing that the choice of scheme has a notable impact on GHI forecasts.

In addition to general performance evaluations, further studies have investigated specific aspects of WRF-Solar. Among them, several studies have focused on the role of aerosols in affecting radiation: Choudhury [35] assessed the impact of time-varying aerosol optical depth (AOD) data on solar irradiance forecasts, demonstrating improved accuracy under varying atmospheric conditions; similarly, Lee et al. [36] examined the impact of different AOD datasets on clear-sky irradiance forecasts produced by WRF-Solar, highlighting that accurate AOD inputs are crucial for improving solar irradiance predictions; Cheng et al. [37] integrated time-varying satellite-based AOD data into WRF-Solar, leading to improved solar irradiance forecasts. In addition, as part of efforts to incorporate observational data through data assimilation, Gentile et al. [38] applied 3D-Var data assimilation of the Spinning Enhanced Visible and Infrared Imager (SEVIRI) radiances to WRF-Solar, demonstrating its potential to improve solar irradiance forecasts. Moreover, ensemble-based probabilistic forecasting has been employed to quantify uncertainties in solar irradiance forecasts: Yang et al. [39] evaluated the WRF-Solar Ensemble Prediction System (EPS) for cloud mask forecasting, highlighting the potential of ensemble-based approaches to improve the accuracy of solar irradiance forecasts; Kim et al. [40] developed a WRF-Solar Ensemble Prediction System with analog ensemble (AnEn) calibration for solar irradiance forecasting, improving forecast reliability and reducing bias by incorporating ensemble uncertainty; Yang et al. [41] applied tangent linear sensitivity analysis to identify sensitive parameters in WRF-Solar, supporting more efficient ensemble forecasting. Overall, these studies highlight the flexibility of WRF-Solar in addressing diverse forecasting challenges.

Accurate GHI forecasting in South Korea is challenging due to the variability in weather conditions caused by monsoon season and complex mountainous topography. The monsoon season, which occurs in summer, is characterized by cloud cover and heavy rainfall, which not only significantly reduces solar radiation but also increases its variability. In contrast, the non-monsoon period experiences clearer sky conditions, leading to higher and more stable solar radiation. Moreover, geographical diversity of South Korea contributes to substantial regional differences in solar radiation: Inland areas generally receive more stable solar radiation, whereas coastal and mountainous regions experience greater fluctuations due to cloud formation, humidity, and terrain-induced atmospheric processes [42]. These factors highlight the necessity of precise GHI forecasting to ensure the stability and efficiency of PV power systems in South Korea.

Despite the increasing need for accurate solar radiation forecasting, research on WRF-Solar in South Korea remains limited, with even a fundamental evaluation yet to be conducted. Given the distinct seasonal variations and complex topography, assessing the capability of WRF-Solar under these conditions is crucial for improving solar radiation forecasting. Moreover, as dependence on solar power grows, precise and reliable GHI forecasting is essential for ensuring accurate PV output predictions and grid stability.

Therefore, this study evaluates the performance of WRF-Solar for GHI forecasts through comparison with the standard WRF model. Specifically, the effectiveness of specialized physical parameterization schemes in WRF-Solar is examined across different sky conditions. The findings of this study will not only establish a baseline for application of WRF-Solar in South Korea but also contribute to more precise GHI forecasting, ultimately supporting the stability and efficiency of PV power generation.

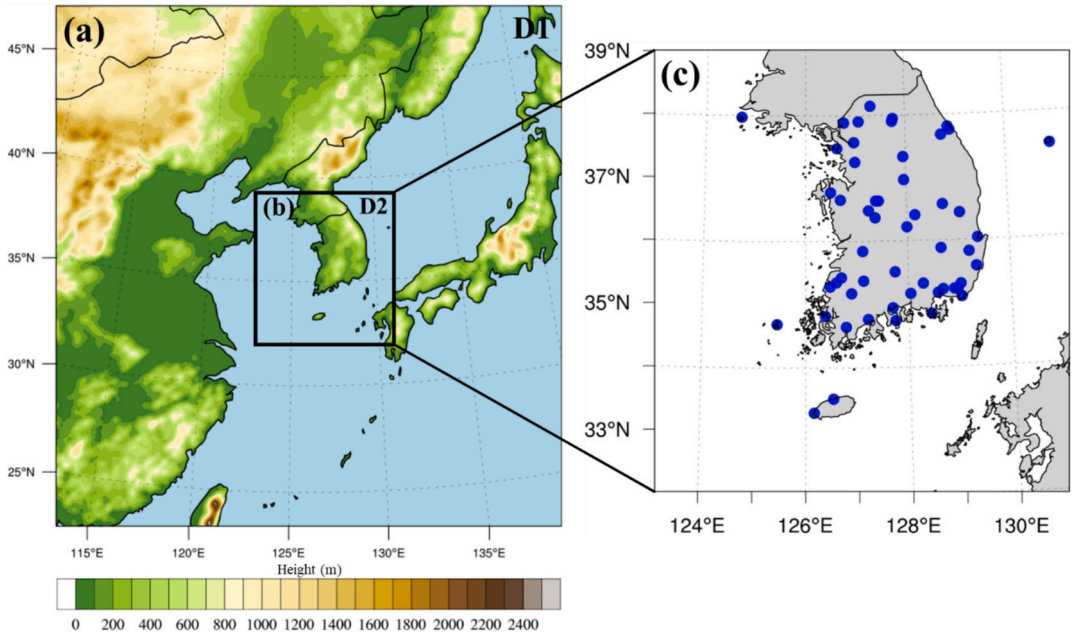


Fig. 1. The model domain with WRF and WRF-Solar for (a) the outer domain (D1), (b) the inner domain (D2), and (c) the locations of the ASOS stations used for the GHI verification: In (c), the blue circles indicate ASOS stations where GHI is observed—a total of 53 sites. (For interpretation of the references to colour in this figure legend, the reader is referred to the web version of this article.)

2. Methodology

2.1. Study area

South Korea is located in East Asia, positioned between approximately 33°N to 43°N and 124°E to 132°E (see Fig. 1a). It experiences a temperate monsoon climate with four distinct seasons, which are characterized by significant seasonal variations in temperature and precipitation [43]. In addition to these climatic factors, the complex topography of South Korea plays a crucial role in affecting the variability in solar resource availability, directly affecting PV power generation.

During summer (June to August), solar radiation typically peaks; however, considerable fluctuations occur due to the monsoon season, which generally lasts from late June to mid-July and is known as Changma in South Korea [44,45]. During this period, cloudy conditions and heavy rainfall can significantly reduce the solar radiation reaching the surface. Conversely, the non-monsoon season is characterized by predominantly clear sky conditions, allowing for more stable and intense solar radiation.

In addition to seasonal variations, the diverse topography of South Korea further influences solar radiation distribution, leading to notable spatial variability. Inland plains receive relatively stable solar radiation, while coastal and mountainous regions experience greater fluctuations due to frequent cloud formation, humidity, and terrain-induced atmospheric processes. The Taebaek and Sobaek mountains, the largest mountain ranges in South Korea, act as natural barriers, influencing local cloud dynamics and solar energy distribution [46].

Such seasonal and geographical variations in solar radiation influence atmospheric processes and energy budgets, thereby impacting the accuracy of GHI forecasts in NWP models. Given that accurate GHI forecasting is essential for optimizing PV power generation, improving the representation of these variations in NWP models is critical for both weather prediction and solar energy applications.

2.2. WRF-Solar model

The Weather Research and Forecasting (WRF) model is an advanced NWP system designed for both research and operational forecasting [47]. It provides a flexible and scalable framework that can simulate various atmospheric processes, including severe weather events, climate simulations, air quality modeling, and solar radiation forecasting. The model supports various spatial and temporal scales, ranging from meters to hundreds of kilometers and minutes to months, making it suitable for diverse applications [48–50]. In addition, WRF offers a comprehensive suite of physical parameterization schemes (options) to represent key atmospheric processes, including land surface, planetary boundary layer, microphysics, cumulus, and radiation [51]. These schemes can be selected according to research objectives and specific targets—regions, weather phenomena, seasons, etc. The selection of appropriate parameterization schemes significantly influences forecasting accuracy, emphasizing the importance of choosing an optimal combination suited to the specific application [52,53].

WRF-Solar is the first NWP model specifically developed to address the increasing demand for specialized numerical forecast products for solar power applications. It was designed as an enhanced version of WRF, incorporating advanced physical parameterization schemes to improve the representation of solar radiation-related processes. The key advancements of WRF-Solar are as follows: 1) The Fast All-sky Radiation Model for Solar Applications (FARMS) shortwave radiation scheme was implemented to enhance the efficiency and accuracy of solar radiation forecasting by employing a computationally efficient radiative transfer code instead of complex mathematical algorithms [54]. It serves as the radiation scheme of WRF-Solar that efficiently computes solar radiation by considering cloud optical properties; 2) The Thompson–Eidhammer (T-E) scheme was applied to improve the representation of aerosol–cloud microphysics interactions, particularly regarding cloud evolution and radiative properties—aerosol indirect effects [55]. It utilizes three-dimensional monthly climatology of the aerosol number concentrations for both hygroscopic and non-hygroscopic aerosols generated by the Goddard Chemistry Aerosol Radiation and Transport (GOCART) model [56]; 3) The Deng shallow cumulus scheme has been implemented to account for subgrid-scale cloud feedback on shortwave radiation, improving representation of cloud fractions [57,58]. Accurately representing unresolved clouds at the subgrid scale is critical for enhancing solar radiation forecasting in NWP models [19]. It considers both deep and shallow convection and has demonstrated to be

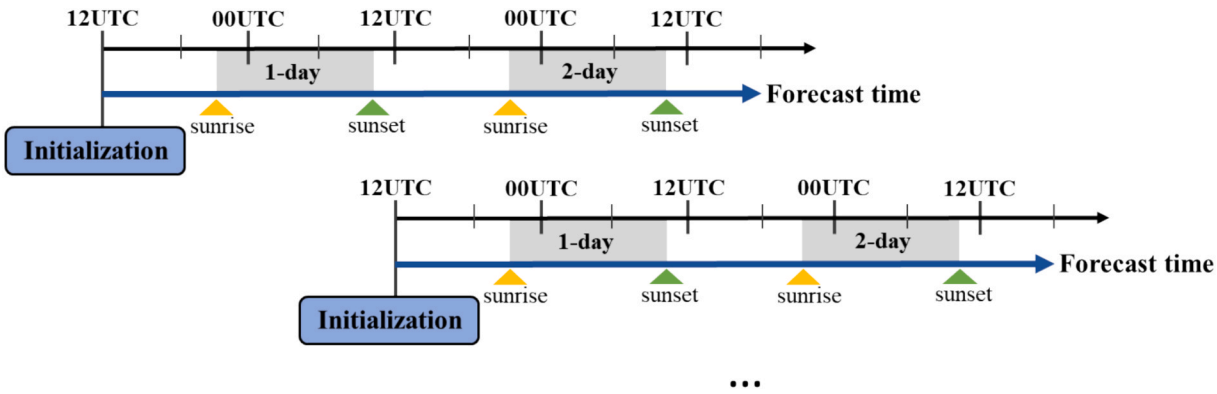


Fig. 2. Schematic representation of the forecast initialization and periods for the 1-day and 2-day forecasts. The model is initialized daily at 1200 UTC and runs for up to 54 h. The gray-shaded areas represent the verification windows, corresponding to daytime hours from sunrise to sunset. The daytime period of the first day is referred to as "1-day," and that of the second day is referred to as "2-day," focusing on the hours when solar irradiance is present.

Table 1
Overview of physical parameterization schemes used in three experiments: CNTL is based on WRF, whereas EXP_R and EXP_F are based on WRF-Solar. Both EXP_R and EXP_F employ the Thompson–Eidhammer microphysics and Deng shallow cumulus schemes; EXP_R adopts the RRTMG shortwave radiation scheme, whereas EXP_F employs the FARMS shortwave radiation scheme. The outer domain (D1) employs the Kain Fritsch (KF) cumulus scheme in all experiments, whereas the inner domain (D2) applies Deng shallow cumulus scheme in WRF-Solar-based experiments.

Schemes	CNTL	EXP_R	EXP_F
Microphysics	Thompson	Thompson–Eidhammer	Thompson–Eidhammer
Cumulus	Kain Fritsch (D1)	Kain Fritsch (D1)	Kain Fritsch (D1)
Shallow cumulus	–	Deng (D2)	Deng (D2)
Shortwave radiation	RRTMG	RRTMG	FARMS
Longwave radiation	RRTMG	RRTMG	RRTMG
PBL	MYNN2	MYNN2	MYNN2
Surface layer	Revised MM5	Revised MM5	Revised MM5
Land surface	Noah	Noah	Noah

particularly effective for high-resolution solar radiation forecasting [30]; 4) A new parameterization was developed to enhance the representation of aerosol direct effects—radiation absorption and scattering—thus better accounting for the high spatiotemporal variability of aerosols [59]. This approach enables WRF-Solar to ingest time-varying aerosol optical properties, allowing for a more accurate simulation of solar radiation variations influenced by aerosols.

Therefore, in South Korea, the performance of WRF-Solar should be evaluated by comparing its solar radiation forecasts—enhanced through specialized physical parameterization schemes—with those of the standard WRF model. This comparison emphasizes the improvements brought by these advanced schemes and enables the identification and correction of biases and errors in WRF-Solar, especially considering the complex topography and climatological conditions of South Korea. These enhancements are vital for improving solar radiation forecasting, which directly impact PV power generation and grid integration.

2.3. Model configuration

This study uses WRF and WRF-Solar version 4.4.2, with two nested domains covering South Korea (see Fig. 1a and 1b). The outer domain (D1) has a spatial resolution of 15 km and a grid of 180 x 185 points. The inner domain (D2) has a higher spatial resolution of 3 km and a grid of 241 x 256 points. South Korea is located within the westerlies, which primarily drive weather systems (e.g., cloud bands) from west to east. Therefore, the western boundary of D2 extends farther than the eastern boundary, considering numerical instabilities at the NWP model boundaries [60] (see Fig. 1b). In the vertical, 45 levels extend to the model top at 50 hPa. The initial and boundary conditions are derived from the Global Forecast System (GFS), with 0.25° × 0.25° resolution, provided by the National Centers for Environmental Prediction (NCEP); the boundary conditions are updated every 6 h. The model was initialized daily at 1200 UTC and runs for up to 54 h, covering 2 days ahead, for the summer of 2023 (June to August). The time step of model was set to 30 s, considering the domain size, horizontal and vertical resolutions, and computational performance. The model output was saved at 1-hour intervals.

Fig. 2 shows the 54-hour forecast timeline, beginning with the model initialization at 1200 UTC. The gray-shaded areas indicate the verification windows—the periods from sunrise to sunset. During summer, sunrise typically occurs between 2100 and 2200 UTC (0600 and 0700 LST), while sunset usually falls between 1000 and 1100 UTC (1900 and 2000 LST). Accordingly, this study designates the daytime period of the first day as "1-day" and that of the second day as "2-day" to assess the solar radiation forecasts during daylight hours. Distinguishing between 1-day and 2-day forecasts is particularly important, as forecast uncertainty in NWP models increases with lead time, leading to larger forecast errors [61]. This increasing uncertainty presents challenges for power planning, highlighting the need for more accurate GHI forecasting to support efficient energy management.

2.4. Experiment design

As mentioned earlier, the choice of physical parameterization schemes in the WRF models, including WRF-Solar, is a crucial factor in determining forecast performance. Therefore, three experiments—CNTL, based on WRF, and EXP_R and EXP_F, based on WRF-Solar—were conducted to assess the performance of the specialized schemes in WRF-Solar by comparing its GHI forecast accuracy with that of WRF.

The physical parameterization schemes employed in this study are summarized in Table 1. All experiments employed the following common schemes: the Mellor–Yamada–Nakanishi–Niino (MYNN) level 2.5 boundary layer scheme [62], the revised Fifth-Generation NCAR/Penn State Mesoscale Model (MM5) surface layer scheme [63], the Noah land surface scheme [64], Rapid Radiative Transfer Model for General Circulation Models (RRTMG) for longwave radiation [65], and the Kain Fritsch (KF) cumulus scheme [66]. The KF scheme is typically used in WRF-Solar studies [34,67]. Here, the application of the cumulus scheme is dependent on the model resolution. In convection-permitting mode, where the resolution is 4 km or finer, convective processes are explicitly

Table 2
Statistical metrics used for model evaluation, including mean bias error (MBE), mean absolute error (MAE), root mean square error (RMSE), normalized RMSE (NRMSE), Pearson correlation coefficient (R), and index of agreement (IOA). Here, F_i and O_i represent the forecasted and observed values, respectively, whereas $\overline{F}$ and $\overline{O}$ denote their mean values. N is the total number of data points across all forecast lead times. The maximum (max(O)) and minimum (min(O)) values of the observations are used for normalization.

Full Name	Statistics	Formula
Mean Bias Error	MBE	$MBE = \frac{1}{N}\sum_{i=1}^{N}(F_i - O_i)$
Mean Absolute Error	MAE	$MAE = \frac{1}{N}\sum_{i=1}^{N}(\lvert F_i - O_i\rvert)$
Root Mean Square Error	RMSE	$RMSE = \sqrt{\frac{1}{N}\sum_{i=1}^{N}(F_i - O_i)^2}$
Normalized RMSE	NRMSE	$NRMSE = \frac{RMSE}{\max(O) - \min(O)} \times 100$
Pearson Correlation Coefficient	R	$R = \frac{\sum_{i=1}^{N}(F_i - \overline{F})(O_i - \overline{O})}{\sqrt{\sum_{i=1}^{N}(F_i - \overline{F})^2 \sum_{i=1}^{N}(O_i - \overline{O})^2}}$
Index Of Agreement	IOA	$IOA = 1 - \frac{\sum_{i=1}^{N}(F_i - O_i)^2}{\sum_{i=1}^{N}(\lvert F_i - \overline{O}\rvert + \lvert O_i - \overline{O}\rvert)^2}$

Table 3
Contingency table for cloud occurrence verification. The table categorizes forecasts against observations into four types: a – both the forecast and the observation indicate clear-sky conditions; b – the forecast indicates cloudy-sky conditions, but the observation shows clear-sky conditions; c – the forecast indicates clear-sky conditions, whereas the observation shows cloudy-sky conditions; d – both the forecast and the observation indicate cloudy-sky conditions. For this classification, "cloudy" and "overcast" conditions are grouped into a single cloudy category.

Contingency	Forecast		
Observation	Sky condition	Clear	Cloudy
	Clear	a	b
	Cloudy	c	d

Table 4
Categorical metrics used for cloud occurrence verification. Each metric is derived from the 2 × 2 contingency table constructed using two sky condition categories: clear sky and cloudy sky—the latter includes both cloudy- and overcast-sky conditions.

Full name	Statistic	Formula
Probability of Detection – Clear	POD_clr	$\frac{a}{a+b} \times 100\%$
Probability of Detection – Cloudy	POD_cld	$\frac{d}{c+d} \times 100\%$
False Alarm Ratio – Clear	FAR_clr	$\frac{c}{a+c} \times 100\%$
False Alarm Ratio – Cloudy	FAR_cld	$\frac{b}{b+d} \times 100\%$
Hit Rate	HR	$\frac{a+d}{a+b+c+d} \times 100\%$
Kuiper's Skill Score	KSS	$\frac{(a \times d) - (b \times c)}{(a+b)(c+d)} \times 100\%$
Mismatched Cloud Frequency	MCF	$\frac{c}{c+d} \times 100\%$

resolved using the microphysics scheme [68]. Consequently, the cumulus scheme was deactivated in D2 at a 3 km resolution. Therefore, the KF cumulus scheme was applied only to D1 in all experiments.

In addition to these common schemes, the specific schemes of each experiment are as follows: 1) CNTL employed the Thompson microphysics scheme and RRTMG scheme for shortwave radiation. For D2, no cumulus scheme was applied; 2) EXP_R used T-E microphysics scheme and RRTMG scheme for shortwave radiation. For D2, Deng shallow cumulus scheme was used; 3) EXP_F applied T-E microphysics scheme and FARMS scheme for shortwave radiation. As with EXP_R, Deng shallow cumulus scheme was used for D2. The key difference between EXP_R and EXP_F is based on their shortwave radiation schemes—EXP_R uses the RRTMG shortwave radiation scheme, whereas EXP_F utilizes the FARMS scheme.

Table 5
The MBE, MAE, RMSE, and IOA for GHI under different sky conditions—ALL, CLR, CLD, and OVC—for CNTL, EXP_R, and EXP_F in the 1-day. Positive MBE values indicate overestimation, whereas negative values indicate underestimation. A higher RMSE value corresponds to a larger error. The MBE, MAE, and RMSE are expressed in $W\ m^{-2}$, while IOA is unitless. The values are averaged over the observational stations (see Fig. 1c).

1-day		MBE	MAE	RMSE	IOA
ALL	CNTL	118.80	166.58	230.19	0.858
	EXP_R	62.24	145.27	199.60	0.881
	EXP_F	13.37	134.63	185.14	0.895
CLR	CNTL	95.30	140.62	186.38	0.888
	EXP_R	40.19	129.77	172.91	0.896
	EXP_F	4.46	130.00	173.79	0.890
CLD	CNTL	173.36	238.44	303.44	0.671
	EXP_R	103.36	197.79	256.40	0.702
	EXP_F	37.06	176.87	232.92	0.724
OVC	CNTL	137.84	177.10	265.91	0.440
	EXP_R	89.17	142.88	212.93	0.492
	EXP_F	17.86	109.90	167.55	0.552

2.5. Evaluation method and data

2.5.1. Statistical error metrics

To evaluate the performance of the experiments, six statistical metrics were employed: Mean Bias Error (MBE), Mean Absolute Error (MAE), Root Mean Square Error (RMSE), Normalized Root Mean Square Error (NRMSE), Pearson correlation coefficient (R), and Index of Agreement (IOA). These metrics offer a comprehensive assessment of accuracy, bias, and overall forecast performance of each experiment (Table 2). The key characteristics of each metric are as follows: 1) Mean Bias Error (MBE) quantifies the average bias in predictions, indicating whether the model systematically overestimates or underestimates the predictions relative to observed values. A positive MBE suggests overestimation, whereas a negative MBE indicates underestimation; 2) Mean Absolute Error (MAE) quantifies the average magnitude of absolute errors between the predicted and observed values, offering an intuitive measure of overall accuracy without considering error direction; 3) Root Mean Square Error (RMSE) assesses the prediction performance of the model by assigning greater weight to larger errors due to squaring. This metric is particularly useful for identifying substantial errors in predictions; 4) Normalized Root Mean Square Error (NRMSE) is obtained by normalizing using the difference between the maximum and minimum observed values, allowing for a relative comparison of error magnitudes across different datasets or models; 5) Pearson Correlation Coefficient (R) quantifies the linear relationship between predicted and observed values. A value close to 1 indicates a strong positive correlation, a value close to −1 represents a strong negative correlation, and a value near 0 suggests little to no correlation. In general, correlation strength is classified as follows: weak ($|R| < 0.3$), moderate ($0.3 \leq |R| < 0.7$), and strong ($|R| \geq 0.7$); 6) Index of Agreement (IOA) quantifies the forecast accuracy by comparing errors to the observed variability, providing a measure of agreement between predicted and observed values. It ranges from 0 to 1, where higher values indicate better model performance.

By employing various evaluation metrics, the forecast performance of the model can be comprehensively assessed in terms of both accuracy and reliability.

Since lower MBE and RMSE indicate improved performance, the improvement rates of these metrics serve as useful indicators for assessing model accuracy. Therefore, the improvement rates (IR) of EXP_R and EXP_F relative to CNTL were calculated for MBE (IR_{MBE}) and RMSE (IR_{RMSE}) as follows:

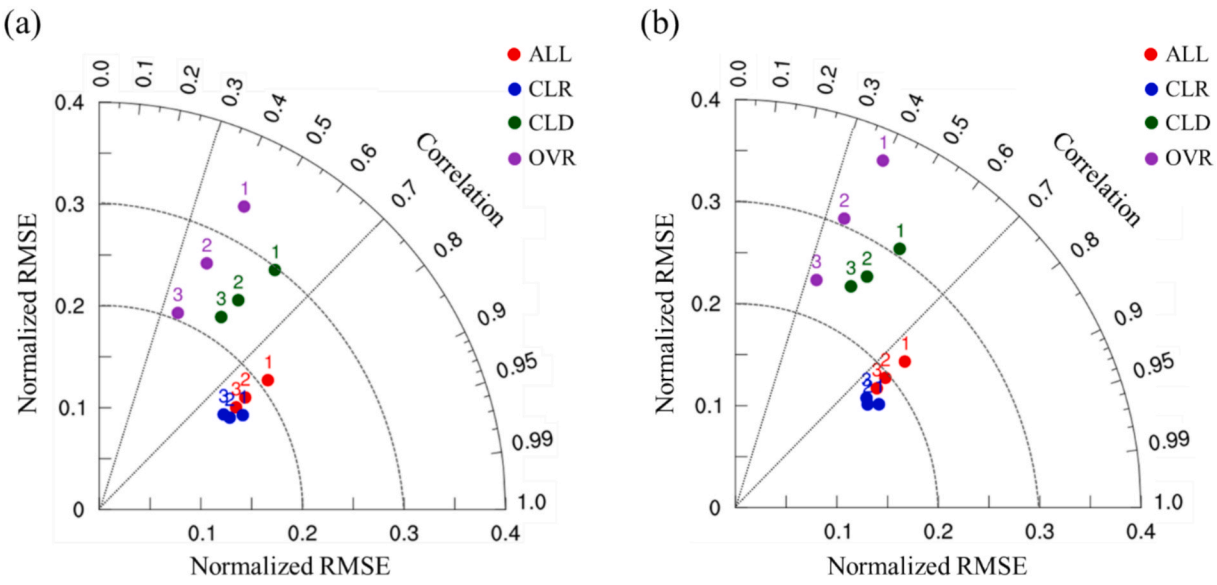


Fig. 3. Taylor diagrams for all experiments using Pearson correlation coefficients (R) and normalized RMSE (NRMSE) for GHI in (a) 1-day and (b) 2-day forecasts. Colored circles represent the sky conditions: All (ALL; red), Clear (CLR; blue), Cloudy (CLD; green), and Overcast (OVR; purple). Numbers above the circles indicate the experiments: 1 for CNTL, 2 for EXP_R, and 3 for EXP_F. The values are averaged over domain 2 (D2) (see Fig. 1c). (For interpretation of the references to colour in this figure legend, the reader is referred to the web version of this article.)

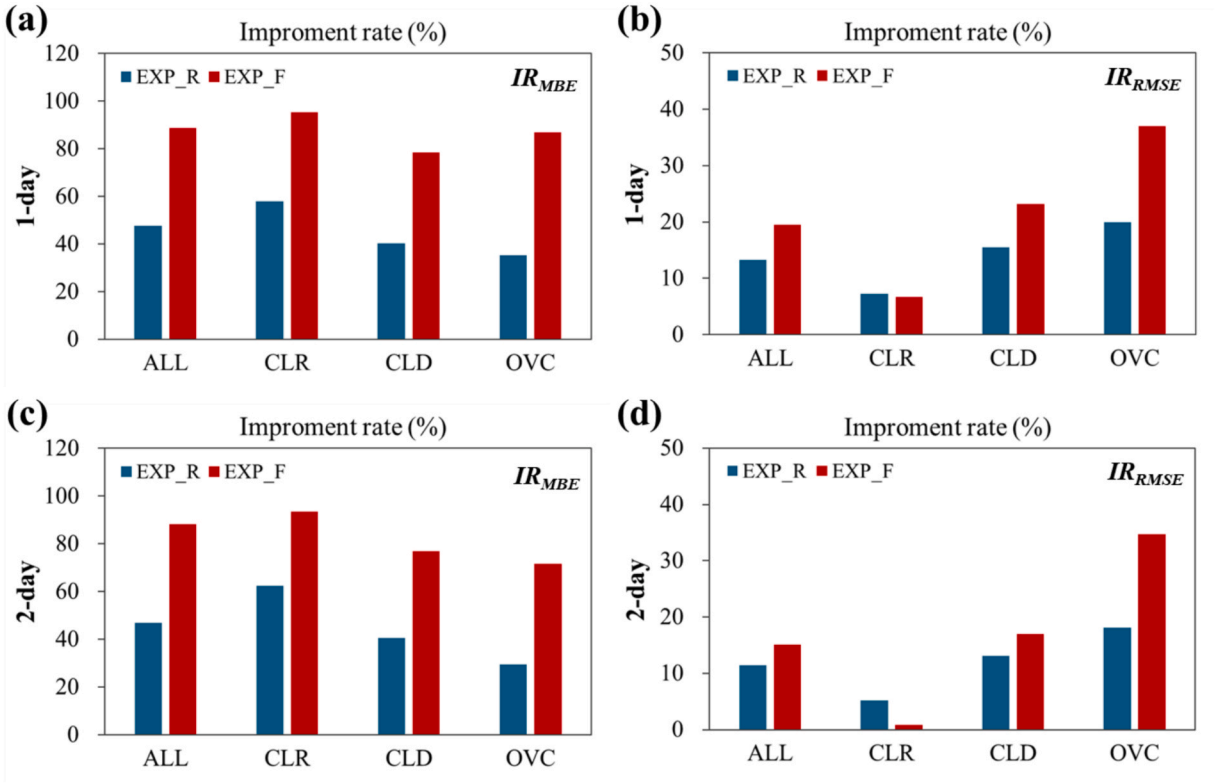


Fig. 4. Improvement rates (IR_{MBE} and IR_{RMSE}; in %) of EXP_R and EXP_F over CNTL for GHI, using surface observation data under different sky conditions—ALL, CLR, CLD, and OVC—are represented for (a) MBE for 1-day, (b) RMSE for 1-day, (c) MBE for 2-day, and (d) RMSE for 2-day. The values are averaged over the inner domain (D2) (see Fig. 1c).

$$IR_{MBE} = \frac{|CNTL_{MBE}| - |EXP_{MBE}|}{|CNTL_{MBE}|} \times 100 \quad (1)$$

$$IR_{RMSE} = \frac{CNTL_{RMSE} - EXP_{RMSE}}{CNTL_{RMSE}} \times 100 \quad (2)$$

Here, IR_{MBE} was calculated using the absolute values of MBE, focusing solely on the magnitude of the bias without considering its direction. Positive values of IR_{MBE} and IR_{RMSE} indicate an improvement over CNTL, whereas negative values suggest the opposite.

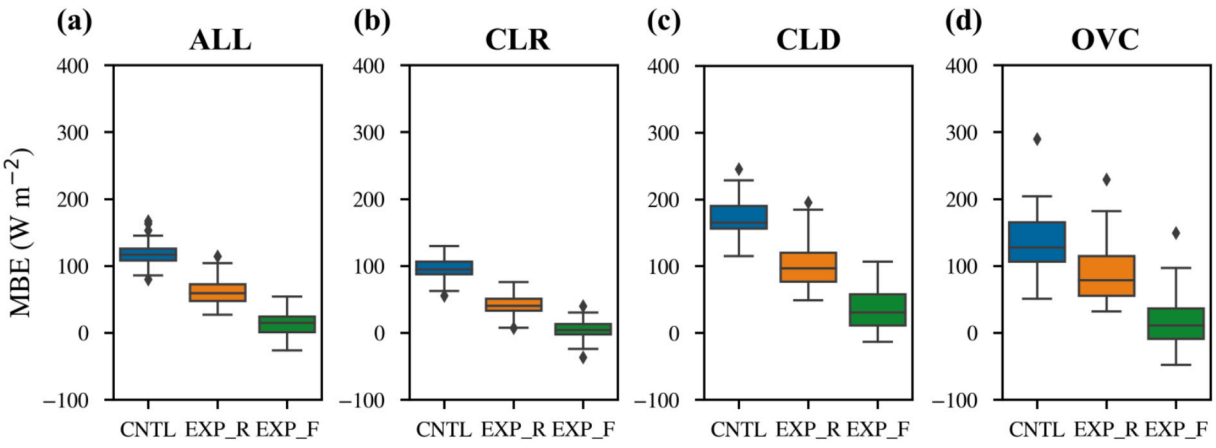


Fig. 5. Boxplots of site-specific MBE for GHI (in $W\,m^{-2}$) under different sky conditions for the 1-day forecasts: (a) ALL, (b) CLR, (c) CLD, and (d) OVC. The central line in each box represents the median (50th percentile), while the box edges indicate the interquartile range (IQR, 25th–75th percentiles), reflecting the variability of site-specific MBE values around the median. The whiskers extend to the minimum and maximum values within 1.5 times the IQR, while data points beyond this range are considered outliers.

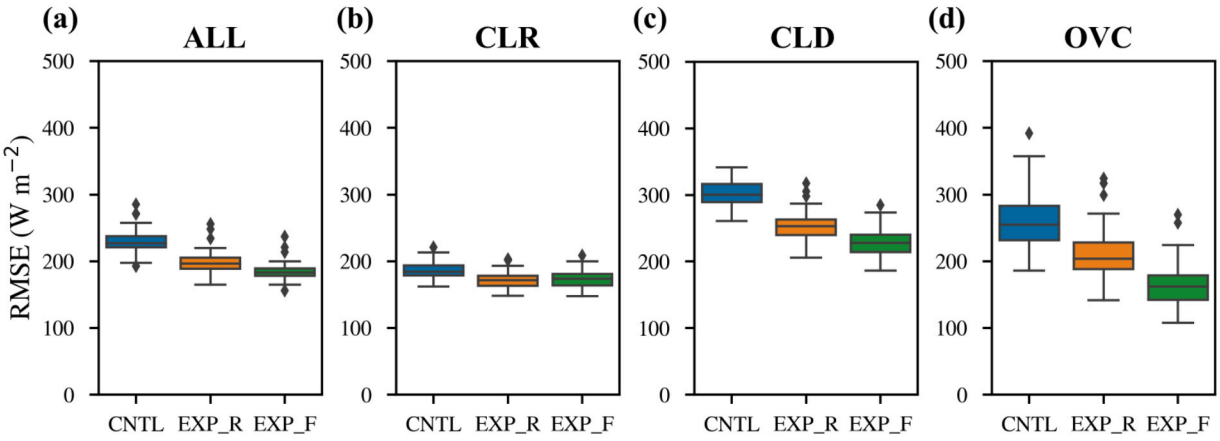


Fig. 6. Same as in Fig. 5 but for RMSE.

2.5.2. Categorical metrics

Since clouds are among the most influential factors affecting surface solar irradiance, the performance of NWP-based solar irradiance forecasts is highly sensitive to the accuracy of cloud detection forecasts. Therefore, to investigate the differences in GHI forecast performance among the experiments, it is essential to assess the reliability of cloud detection forecasts in each experiment.

In this study, we adopted the verification method for cloud occurrence proposed by Yang et al. (2022) [39]. The forecasts and observations were classified into clear (cloud-free) and cloud occurrences—the latter including both CLD and OVC. Based on this classification, the four categories of the 2 × 2 contingency table (Table 3) were defined as follows: a – both the forecast and the observation indicate cloudy-sky occurrences; b – the forecast predicts cloudy-sky occurrences, whereas the observation shows clear-sky occurrences; c – the forecast shows clear-sky occurrences, but the observation indicates cloudy-sky occurrences; d – both the forecast and the observation indicate cloudy-sky occurrences.

These categories were then used to compute categorical metrics (Table 4): Probability of Detection (POD) is the proportion of observed clear-sky (POD_clr) or cloudy-sky (POD_cld) occurrences that were correctly forecast; False Alarm Ratio (FAR) is the proportion of forecasted clear-sky (FAR_clr) or cloudy-sky (FAR_cld) occurrences that did not occur; Hit Rate (HR) indicates the overall proportion of correct forecasts for both clear- and cloudy-sky occurrences; Kuiper's Skill Score (KSS) accounts for both HR and FAR to reduce bias under class-imbalanced conditions, such as when clear or cloudy occurrences dominate (e.g., "a" or "d" in Table 3). The five metrics, except for KSS, range from 0 % to 100 %, where 0 % indicates no forecast skill and 100 % denotes perfect forecast. KSS range from –100 % to 100 %, where values ≤ 0 % indicate no skill and 100 % indicates a perfect forecast; Mismatched Cloud Frequency (MCF) is used as a complementary metric that quantifies the frequency of mismatched cloud forecasts—defined as 100 % minus POD_cld.

2.5.3. Classification of sky conditions

To evaluate the performance of GHI forecasting across all experiments, sky conditions were classified based on the influences of aerosols and clouds. This classification was determined using the clearness index (K_t), defined as the ratio of observed GHI (I) to the clear-sky GHI (I_{cs}) as follows:

$$K_t = \frac{I}{I_{cs}} \tag{3}$$

where I represents surface-observed GHI, and I_{cs} denotes the clear sky GHI calculated using the Ineichen and Perez clear sky model [69,70]. The K_t is used to classify daily average sky conditions [71,72].

Following previous studies [73,74], sky conditions were classified into three categories based on K_t values: clear ($K_t \geq 0.65$), cloudy ($0.35 \leq K_t < 0.65$), and overcast ($K_t < 0.35$). Using this classification, sky

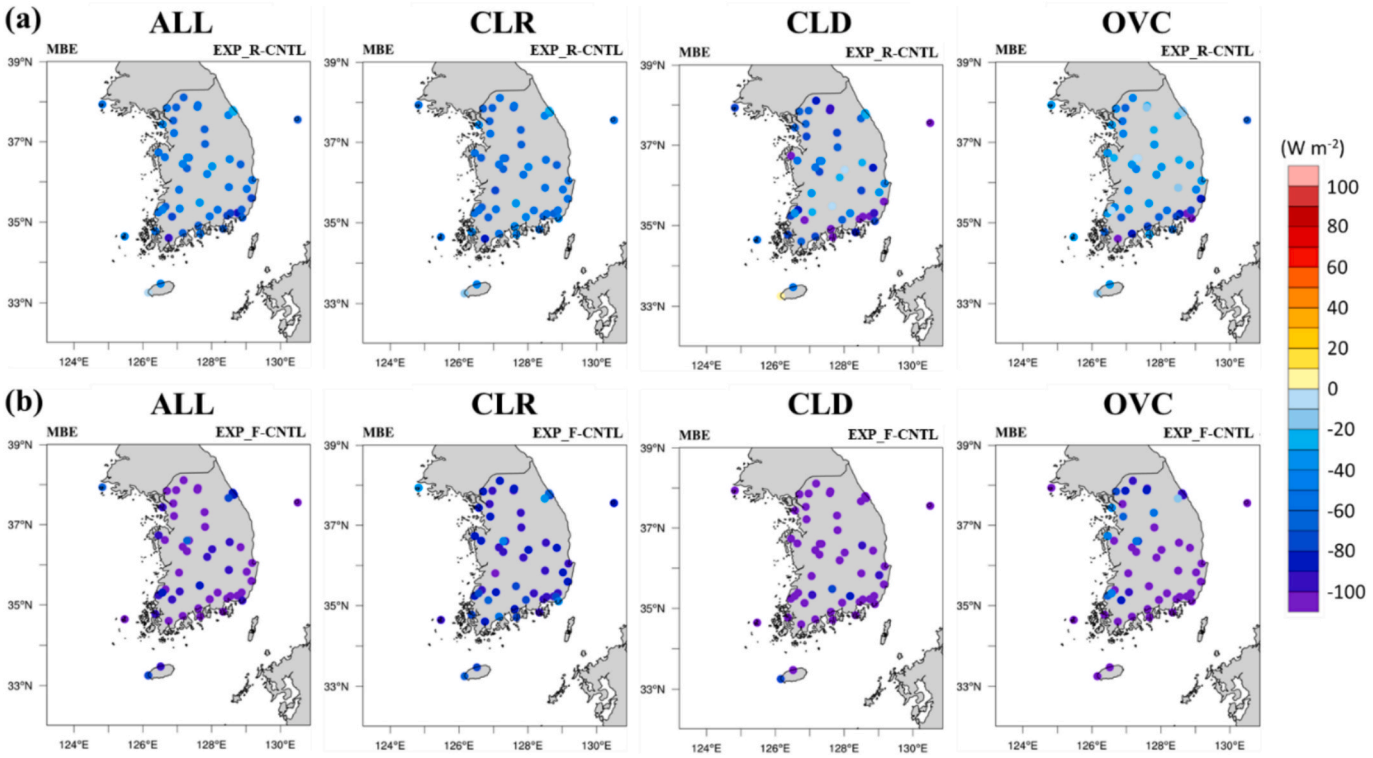


Fig. 7. Horizontal distribution of the MBE differences between WRF (CNTL) and WRF-Solar (EXP_R and EXP_F) for GHI (in $W\ m^{-2}$) under different sky conditions—ALL, CLR, CLD, and OVC—for the 1-day forecasts: (a) for EXP_R minus CNTL; (b) for EXP_F minus CNTL. The stations with negative values (cold colors) indicate that EXP_R or EXP_F are superior to CNTL, while those with positive values (warm colors) demonstrate that the former is inferior to the latter.

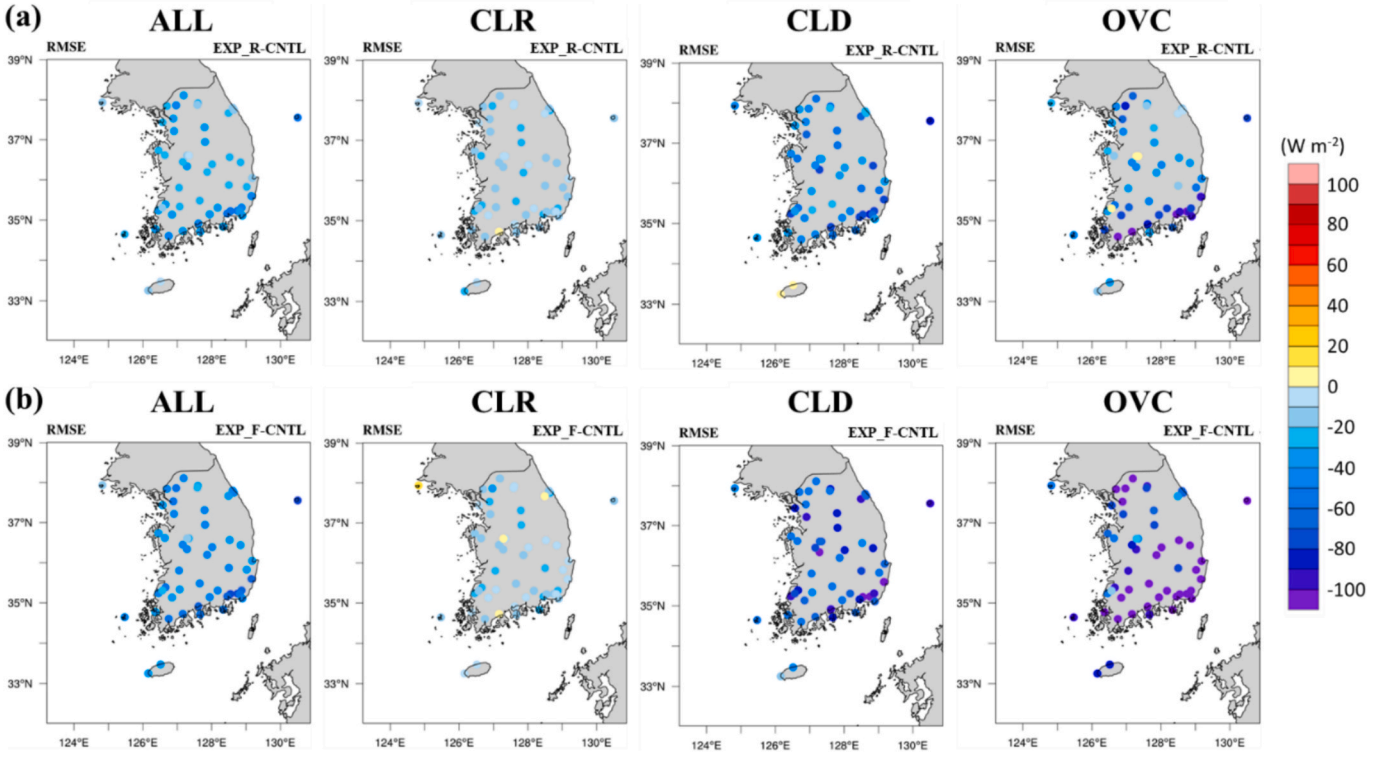


Fig. 8. Same as in Fig. 7 but for RMSE.

conditions during the summer of 2023 were analyzed. Clear sky conditions (CLR) were the most frequent, occurring in 60.2 %, followed by cloudy sky conditions (CLD) in 18.8 % and overcast sky conditions (OVC) in 21.0 %.

To minimize errors associated with GHI measurements during early morning and late evening, as well as seasonal variations in sunrise and

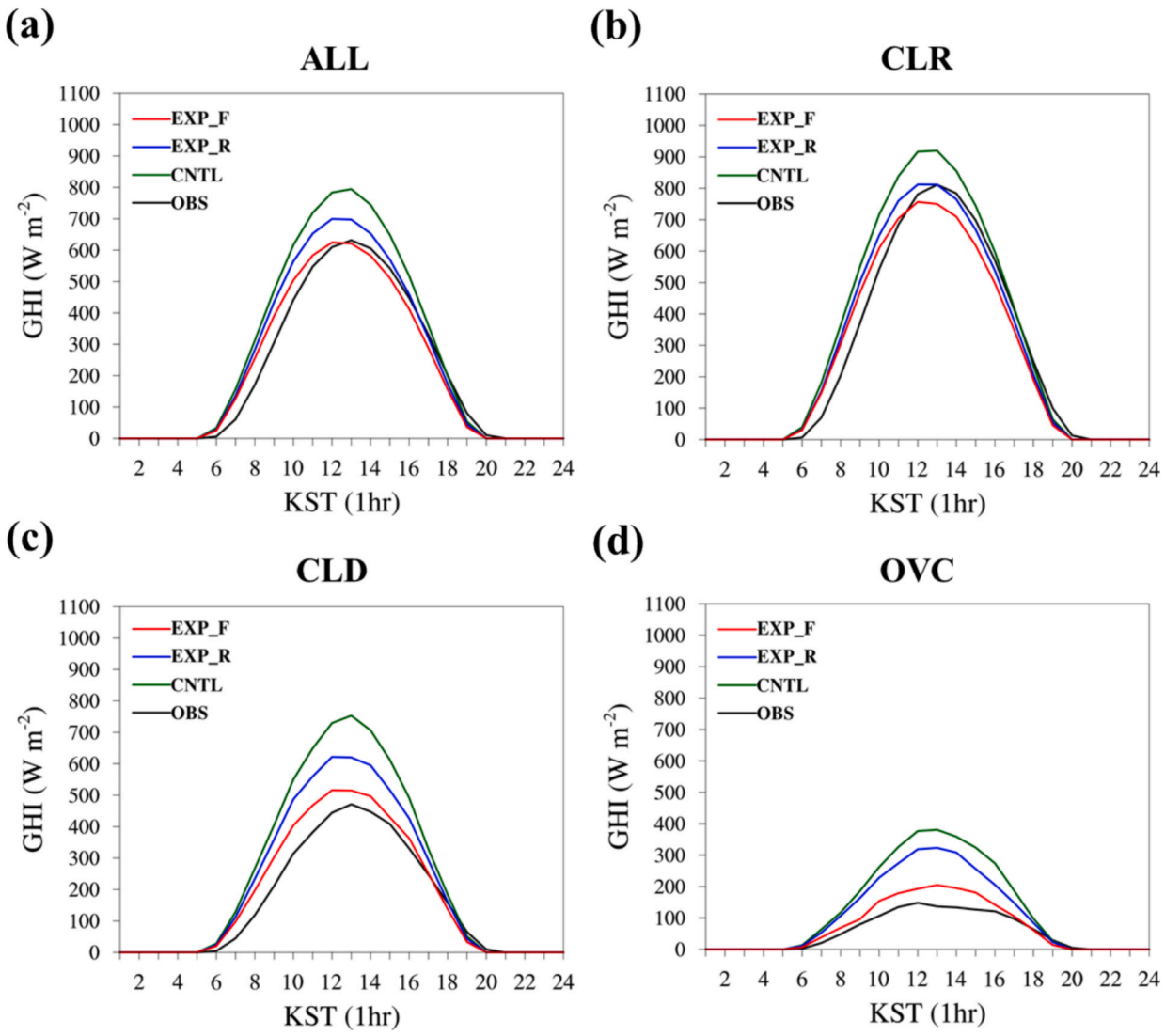


Fig. 9. Average diurnal variation of GHI (in $W\,m^{-2}$) for observation (OBS in black) and different experiments (CNTL in green; EXP_R in blue; EXP_F in red) under different sky conditions—(a) ALL, (b) CLR, (c) CLD, and (d) OVC, for the 1-day forecasts during the summer of 2023. (For interpretation of the references to colour in this figure legend, the reader is referred to the web version of this article.)

sunset, the observed and modeled GHI were evaluated only when the solar zenith angle (SZA) was below 80° [36,75].

2.5.4. Surface observation data

GHI, which consists of direct and diffuse solar radiation, is measured every second using 53 pyranometers deployed nationwide at Automated Surface Observing System (ASOS) stations, operated by the Korea Meteorological Administration (KMA). These measurements are averaged over 60 s and recorded at 1-minute intervals. The collected data are processed through quality control, and an hourly representative value is computed by averaging the previous hour's data [76].

This study analyzed 1-hour interval GHI data from 53 ASOS stations during the summer of 2023 (June to August) (see Fig. 1c). To ensure data quality, GHI measurements were excluded when the SZA exceeded 80°, the sun was below the horizon, or data were missing.

2.5.5. Remote sensing data

The Moderate Resolution Imaging Spectroradiometer (MODIS) is an instrument onboard the Terra (launched in 1999) and Aqua (launched in 2002) satellites [77] under the Earth Observing System (EOS) program of the National Aeronautics and Space Administration (NASA). Each satellite is equipped with a MODIS instrument, which observes the Earth's atmosphere, clouds, aerosols, oceans, and land surfaces, supporting long-term research on global environmental changes. In this study, GHI data were obtained from the MCD18A1 Version 6.2 dataset with a spatial resolution of 1 km, which provides a Downward Shortwave Radiation (DSR) product derived from MODIS. This product offers instantaneous DSR at the time of each MODIS overpass, with data available at approximately 3-hour intervals, representing the solar radiation incident on land surfaces within the shortwave spectrum (300–4,000 nm). The DSR retrieval algorithm first derives surface reflectance from multi-temporal signatures of MODIS observations. Based on the retrieved reflectance, DSR is then estimated through radiative transfer calculations using look-up tables (LUTs). The LUTs are designed to account for differences in aerosol and cloud amounts depending on solar angle and sensor geometry. Global DSR products are generated using data from both MODIS and geostationary satellites to ensure broad spatial and temporal coverage [78].

The Geostationary Korea Multi-Purpose Satellite-2A (Geo-KOMPSAT-2A; GK2A) is a next-generation geostationary meteorological satellite operated by KMA, positioned at 128.2°E and equipped with the Advanced Meteorological Imager (AMI). AMI provides full-disk observations over the Asia-Pacific region every 10 min and high-resolution observations of the Korean Peninsula every 2 min. This study used

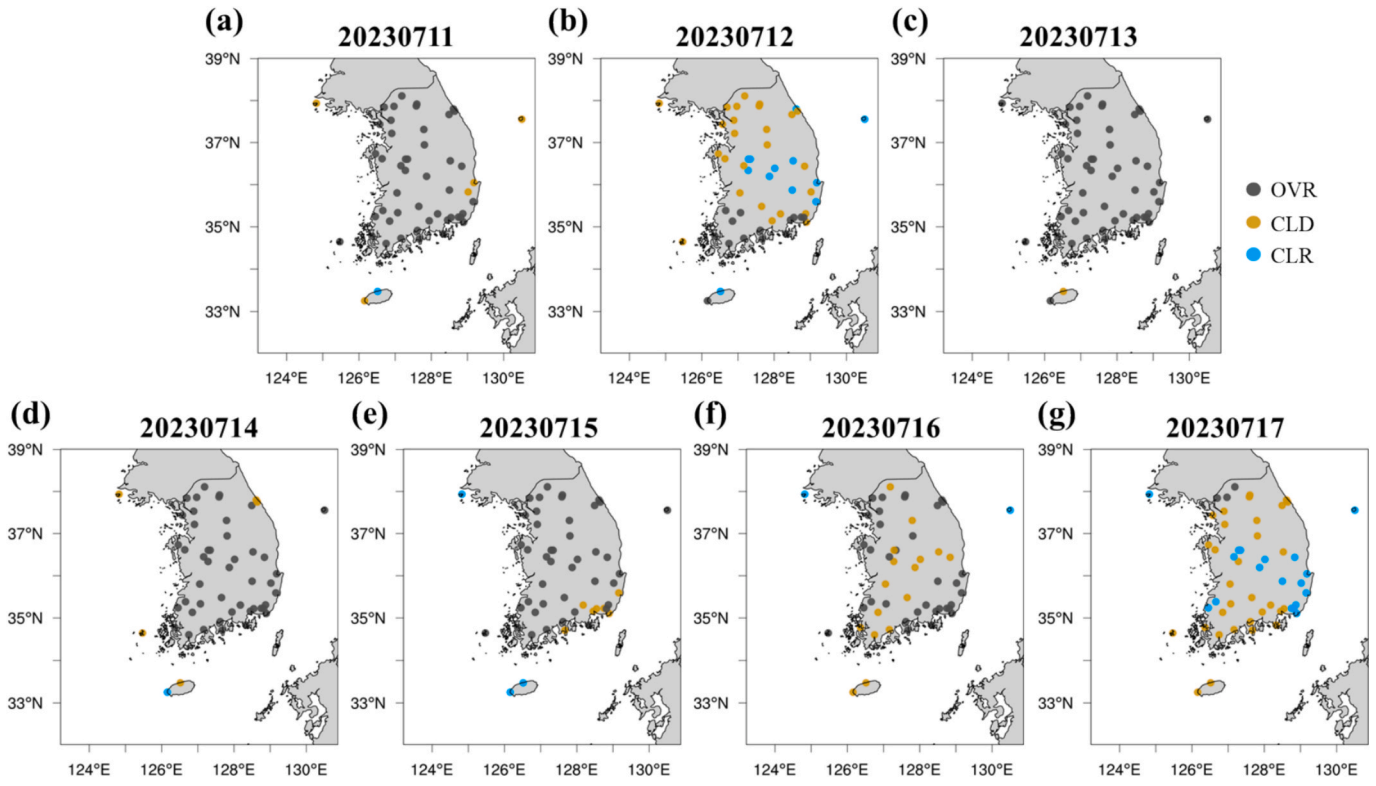


Fig. 10. Sky conditions classified by K_t values during the monsoon season over South Korea, where (a) – (g) represent July 11–17, 2023. The colored circles represent the sky conditions based on K_t values: sky blue dots for clear sky conditions (CLR), ochre for cloudy sky conditions (CLD), and dark gray for overcast sky conditions (OVC). (For interpretation of the references to colour in this figure legend, the reader is referred to the web version of this article.)

DSR and cloud detection data obtained from GK2A/AMI: 1) The DSR product provides surface shortwave radiation at a 2 km resolution every 10 min under all-sky conditions. It is estimated using regression models derived from radiative transfer simulations, incorporating inputs such as surface reflectance, solar geometry, land cover type, and cloud optical properties. The regression coefficients are precomputed using the Santa Barbara DISORT Atmospheric Radiative Transfer (SBDART) model [79] under various atmospheric conditions [80]; 2) The cloud detection product provides a categorical cloud mask that classifies each pixel as "cloud," "probably cloud," or "clear." The underlying algorithm applies a series of threshold-based tests using brightness temperature differences, reflectance ratios, and spatial variability, while accounting for factors such as solar zenith angle, surface type (land or ocean), and regions affected by specular reflection [81]. This product plays a critical role in validating cloud forecasts and serves as a key input for the DSR retrieval algorithm.

3. Results

3.1. Evaluation based on in-situ data

This study assessed the forecast performance of GHI for CNTL, EXP_R, and EXP_F across different sky conditions—CLR, CLD, and OVC—using various evaluation metrics. The analysis also included all-sky conditions (ALL), which encompass CLR, CLD, and OVC. The evaluation was conducted using GHI observations from 53 ASOS stations during the summer of 2023, with separate assessments for 1-day and 2-day forecasts.

3.1.1. Statistical error validation

Table 5 shows MBE, MAE, RMSE (in $W\,m^{-2}$), and IOA of GHI for all experiments under the four sky conditions—ALL, CLR, CLD, and OVC—for both the 1-day and 2-day forecasts. The evaluation of each sky condition in the 1-day forecast is as follows: 1) For ALL, all experiments showed a tendency for overestimation. EXP_F exhibited the smallest MBE, indicating the least bias, followed by EXP_R and CNTL. This trend was also apparent in MAE and RMSE, with EXP_F exhibiting the lowest values, confirming its superior forecast performance, followed by EXP_R and CNTL. Similarly, IOA showed that EXP_F achieved the highest agreement with observations, followed by EXP_R and CNTL; 2) For CLR, EXP_F showed the smallest MBE. However, the differences in MAE, RMSE, and IOA between EXP_R and EXP_F were very small—0.03 $W\,m^{-2}$, 0.88 $W\,m^{-2}$, and −0.006, respectively—indicating that both experiments exhibited very similar performance. Moreover, both showed improved forecast accuracy compared to CNTL. Among the four sky conditions, CLR exhibited the smallest bias and forecast errors; 3) For CLD, EXP_F showed the smallest MBE, followed by EXP_R and CNTL. EXP_F also achieved the lowest MAE and RMSE and the highest IOA, demonstrating the highest forecast accuracy, followed by EXP_R and CNTL. Among the four sky conditions, OVC exhibited the largest bias and forecast errors; 4) For OVC, similar to ALL and CLD, EXP_F demonstrated the best performance in terms of MBE, MAE, RMSE, and IOA, followed by EXP_R and CNTL. Among the four sky conditions, OVC exhibited the lowest IOA.

In the 2-day forecast, MBE remained similar or slightly decreased for ALL, CLR, and CLD compared to the 1-day forecast, whereas it increased for OVC across all experiments. Furthermore, MAE and RMSE increased, while IOA decreased for the four sky conditions across all experiments due to the increasing forecast uncertainty in NWP models with lead time [46].

Overall, EXP_F exhibited the best performance, particularly under cloudy sky conditions (CLD and OVC), and EXP_R also showed notable improvements. These enhancements can be attributed to the specialized physical parameterization schemes in WRF-Solar: EXP_R and EXP_F applied T-E microphysics, and EXP_F additionally used the FARMS shortwave radiation scheme along with these two schemes.

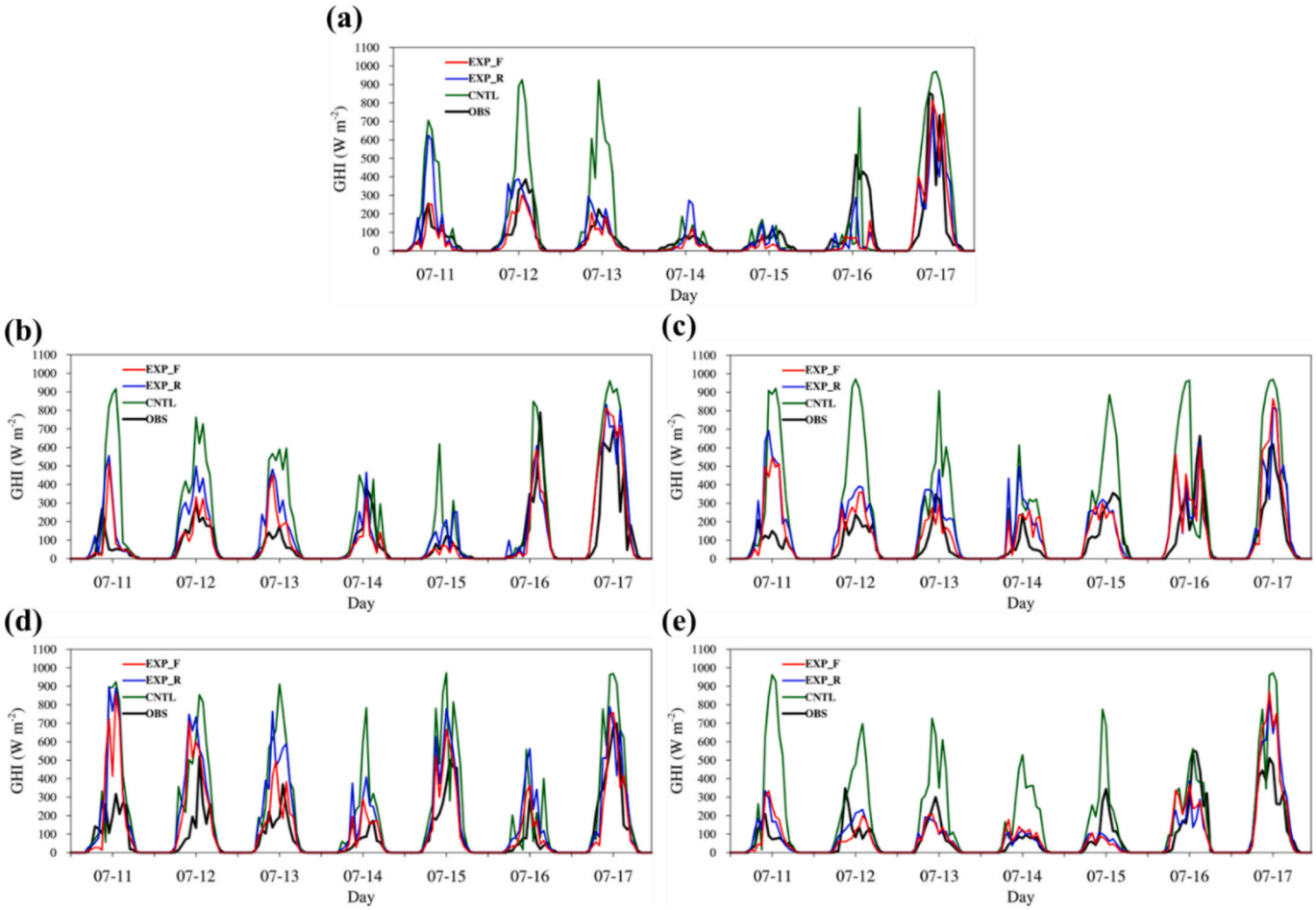


Fig. 11. Diurnal cycle of GHI observation sites in Jeollanam-do during the monsoon season from July 11 to 17, 2023: (a) Gwangju, (b) Mokpo, (c) Boseong, (d) Yeosu, and (e) Gangjin. The black, green, blue, and red lines represent observations, CNTL, EXP_R, and EXP_F, respectively. (For interpretation of the references to colour in this figure legend, the reader is referred to the web version of this article.)

Fig. 3 shows Taylor diagrams depicting the GHI forecast performance of each experiment under different sky conditions based on R and NRMSE. The analysis results for the 1-day forecast are as follows (Fig. 3a): 1) For ALL, all experiments showed a similar R of approximately 0.8, indicating a strong correlation. However, EXP_F had the lowest NRMSE, indicating the highest forecast accuracy, followed by EXP_R and CNTL; 2) For CLR, all experiments showed R above 0.8, similar to ALL, indicating a strong correlation. Among them, CNTL exhibited a slightly higher R value of 0.836 compared to EXP_R and EXP_F. The NRMSE for EXP_R (0.157) and EXP_F (0.158) were nearly identical, resulting in lower errors than CNTL. Compared to CLD and OVR, CLR showed better overall performance, and R and NRMSE showed similar values across the experiments; 3) For CLD, all experiments showed a decreasing trend in R (moderate correlation) and an increasing trend in NRMSE compared to CLR. EXP_F showed the lowest NRMSE, indicating the best forecast performance, followed by EXP_R and CNTL. In terms of R, all experiments were similar; 4) For OVR, all experiments showed a decreasing trend in R (moderate correlation), with the lowest correlation among the four sky conditions. Similar to CLD, EXP_F showed the lowest NRMSE, indicating the highest forecast accuracy, followed by EXP_R and CNTL. All experiments had similar R values.

In the 2-day forecast, the overall trends in R and RMSE were similar to those in the 1-day forecast; however, R decreased while NRMSE increased, resulting in weaker correlation and lower forecast accuracy. As with the 1-day forecast, EXP_F overall showed excellent forecast performance among all experiments under the four sky conditions (Fig. 3b).

In general, EXP_F demonstrated superior forecast performance among all experiments under the four sky conditions, with particularly notable improvements observed under cloudy conditions such as CLD and OVC, even though it exhibited only moderate correlation. This suggests that the combination of specialized schemes in WRF-Solar—such as T-E microphysics scheme, Deng shallow cumulus scheme, and FARMS shortwave radiation scheme—contributed to enhancing the accuracy of GHI forecasts.

Fig. 4 shows IR_{MBE} and IR_{RMSE}, which represents the improvement rates of EXP_R and EXP_F relative to CNTL, in the 1-day and 2-day forecasts. In the 1-day forecast, EXP_R and EXP_F exhibited IR_{MBE} values of approximately 47.6 % and 88.7 % for ALL, 57.8 % and 95.3 % for CLR, 40.4 % and 78.6 % for CLD, and 35.3 % and 87.0 % for OVC, respectively, indicating a notable reduction in mean bias compared to CNTL (Fig. 4a). For IR_{RMSE}, EXP_R and EXP_F improved by 13.3 % and 19.6 % for ALL, 7.2 % and 6.8 % for CLR, 15.5 % and 23.2 % for CLD, and 19.9 % and 37.0 % for OVC, respectively, demonstrating a significant reduction in forecast errors compared to CNTL (Fig. 4b). Overall, both EXP_R and EXP_F exhibited the lowest improvement rates in CLR and the highest in OVC. Additionally, EXP_F achieved the highest IR_{RMSE} of 37.0 % in OVC. EXP_F improved more than EXP_R under CLD and OVC, but they performed similarly under CLR. Considering that EXP_R and EXP_F shared all schemes except for the FARMS shortwave radiation scheme, these results highlight the superior performance of FARMS in WRF-Solar, particularly in regions with frequent cloudy or overcast conditions.

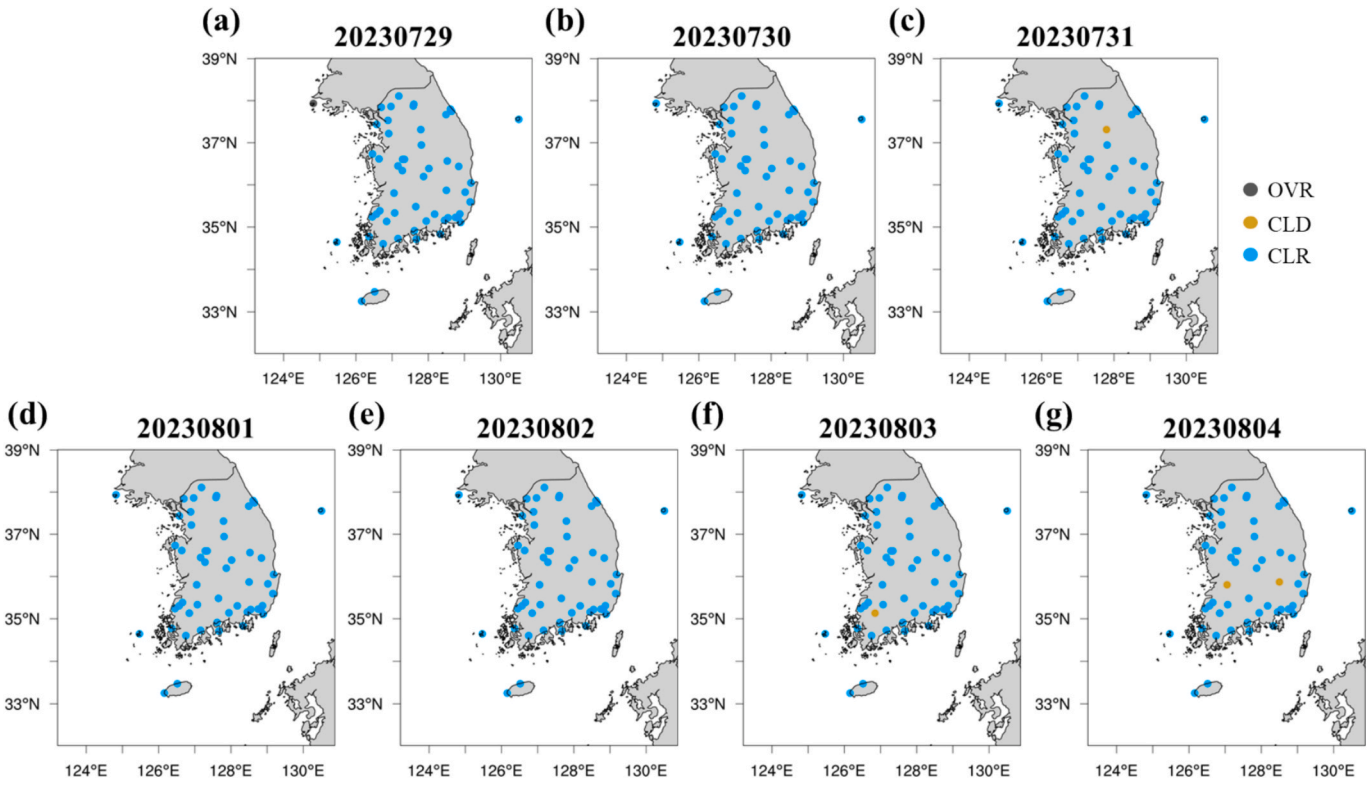


Fig. 12. Same as in Fig. 10 but for the non-monsoon season from July 29 to August 4, 2023.

Fig. 4c and 4d show IR_{MBE} and IR_{RMSE} for the 2-day forecast, respectively. Both IR_{MBE} and IR_{RMSE} showed a slight decrease across the four sky conditions, with EXP_F achieving the highest IR_{RMSE} of 34.7 % in OVC.

Overall, EXP_F showed substantial improvements, particularly under CLD and OVC, reducing RMSE by up to 37.0 % compared to CNTL. EXP_R also showed notable improvements, achieving a maximum RMSE reduction of 19.9 % under OVC. The improvements rates of EXP_R and EXP_F decreased in the 2-day forecast relative to the 1-day forecast. This decline is attributed to the increasing nonlinearity of NWP models over longer forecast periods.

In order to comprehensively evaluate the distribution and spatial variability of forecast bias and errors, site-specific MBE and RMSE are analyzed using boxplots. In a boxplot, the size of the box represents the interquartile range (IQR, 25th–75th percentiles), indicating data variability around the median (50th percentile). The whiskers extend to the minimum and maximum values within 1.5 times the IQR, while data points beyond this range are considered outliers. This approach allows for a quantitative assessment of model performance in terms of systematic bias, forecast error magnitude, and spatial consistency under different sky conditions.

Fig. 5 shows boxplots of MBE from 53 GHI observation sites during summer under the four sky conditions for the 1-day forecast. The detailed analysis is as follows: 1) For ALL, EXP_F exhibited the lowest median, indicating the least forecast bias. In contrast, CNTL had the highest median, indicating the greatest overestimation of GHI. Although its narrow IQR suggested low variability across sites, multiple outliers highlighted significant forecast errors. EXP_R showed more bias than EXP_F but less than CNTL; 2) For CLR, EXP_F had the lowest median, indicating the smallest GHI forecast bias, followed by EXP_R and CNTL. Among the four sky conditions, CLR had the lowest median; 3) For CLD, EXP_F also showed the lowest median; however, it had the widest IQR, suggesting relatively higher spatial variability. In contrast, CNTL showed the highest median, reflecting the largest bias, but its narrowest IQR indicated the lowest spatial variability. Similar to other sky conditions, EXP_R exhibited a bias trend between EXP_F and CNTL; 4) For OVC, EXP_F showed the lowest median. Additionally, its relatively narrow IQR suggested lower spatial variability and more stable performance, followed by EXP_R and CNTL.

Fig. 6 is the same as in Fig. 5 but for RMSE. The detailed analysis is as follows: 1) For ALL, EXP_F had the lowest median, indicating the smallest forecast error. Additionally, it had the narrowest IQR, suggesting low spatial variability and stable performance across observation sites. In contrast, CNTL exhibited the highest median and the widest IQR, reflecting the largest forecast errors and greater spatial variability; 2) For CLR, EXP_R had the lowest median, demonstrating the best forecast performance. However, the RMSE differences among the experiments were small, and the overall RMSE was lower than in other sky conditions. This suggests that the model generally exhibited high forecast accuracy under CLR, with negligible influence cloud effects, including those represented by the specialized schemes in WRF-Solar; 3) For CLD, EXP_F showed the lowest median, indicating the most accurate forecasts, followed by EXP_R and CNTL. In terms of IQR, EXP_R had the narrowest range, suggesting the highest spatial consistency. However, the presence of multiple outliers indicates that forecast errors were relatively large at some sites; 4) For OVC, similar to CLD, EXP_F had the lowest median, demonstrating the best forecast accuracy, followed by EXP_R and CNTL. EXP_F and EXP_R exhibited a narrower IQR than CNTL, indicating the higher spatial consistency.

In the 2-day forecast, both MBE and RMSE exhibited trends similar to those in the 1-day forecast. For MBE, EXP_F consistently showed the smallest MBE across the four sky conditions (Fig. S1). In terms of RMSE, differences among experiments were very small under CLR. However, under CLD and OVC, EXP_F achieved the lowest RMSE, followed by EXP_R and CNTL. Notably, under OVC, EXP_F exhibited a relatively narrower IQR than the other experiments, indicating lower spatial variability and more consistent performance across observation sites (Fig. S2).

Overall, EXP_F exhibited a good performance, consistently achieving the low MBE and RMSE across the four sky conditions, particularly

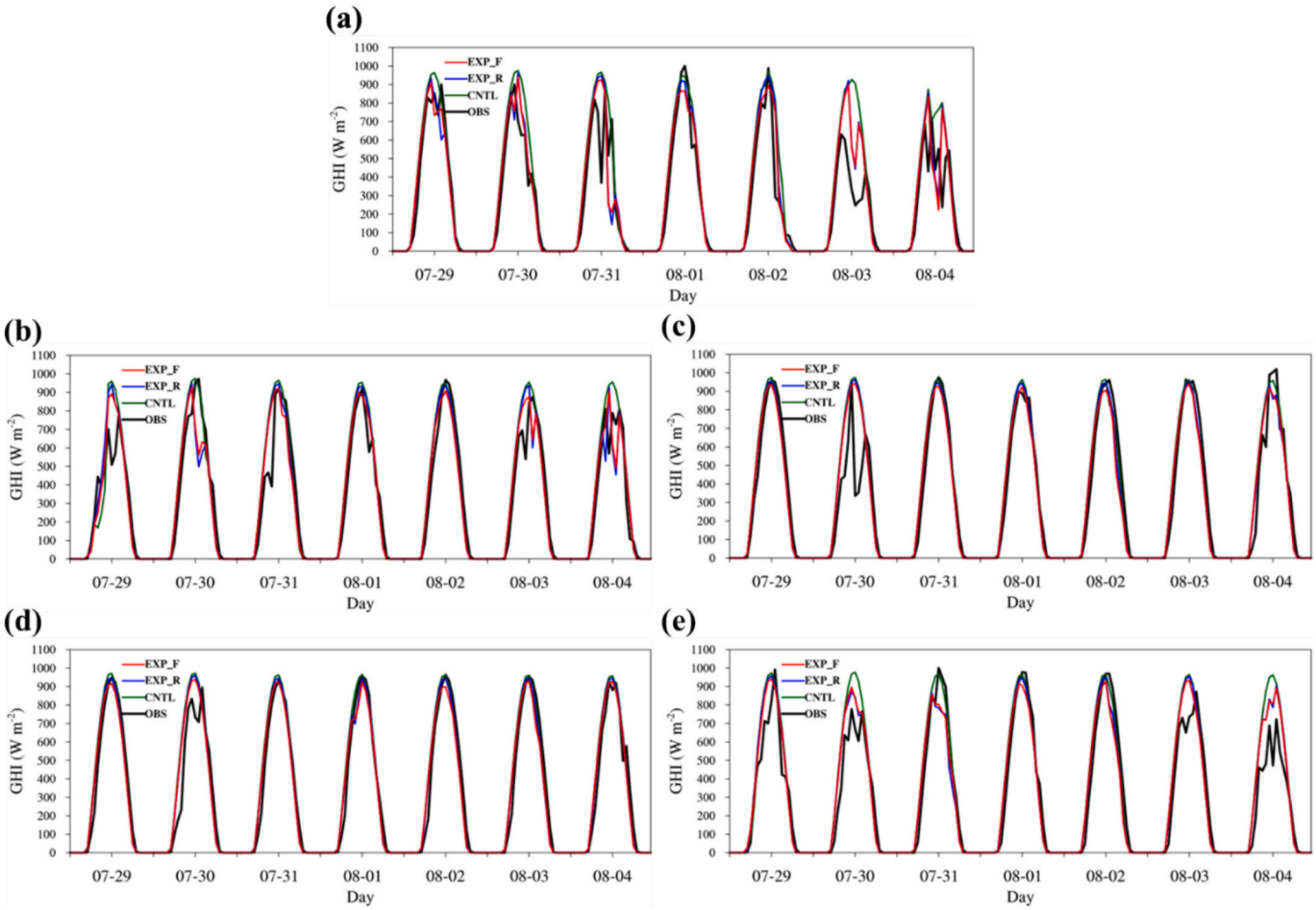


Fig. 13. Same as in Fig. 11 but for the non-monsoon season from July 29 to August 4, 2023.

under CLD and OVC, where it also demonstrated the highest spatial consistency.

3.1.2. *Evaluation by stations*

Even if the overall forecast performance of a NWP model is good, its accuracy may vary across different regions, potentially reducing the reliability of predictions in specific areas. Therefore, evaluating the performance of a NWP model at a regional scale is crucial. In this regard, station-by-station analyses of MBE and RMSE are essential for assessing how well a NWP model captures local characteristics.

Figs. 7 and 8 show the station-by-station distributions of MBE and RMSE differences between EXP_R and CNTL (Fig. 7a and 8a) and between EXP_F and CNTL (Fig. 7b and 8b), respectively, for GHI in the 1-day forecast. Stations with negative values (cool colors) indicate that EXP_R or EXP_F outperform CNTL, whereas those with positive values (warm colors) indicate the opposite. For MBE, except for a single station under CLD in EXP_R, both EXP_R and EXP_F exhibited reduced bias compared to CNTL at all stations. Notably, the bias reduction was more significant in EXP_F (Fig. 7). For RMSE, although error reduction over CNTL was not observed at a few stations, overall improvements were evident in both EXP_R and EXP_F. In addition, under CLR, the error reduction was relatively smaller than CLD and OVC, whereas under OVC, EXP_F showed the most significant error reduction nationwide (Fig. 8).

In the 2-day forecast, MBE exhibited a trend similar to that in the 1-day forecast, with both EXP_R and EXP_F showing reduced bias compared to CNTL across all regions. Notably, the bias reduction was more noticeable in EXP_F (Fig. S3). For RMSE, significant error reductions were observed nationwide in ALL, CLD, and OVC for both EXP_R and EXP_F. However, in CLR, EXP_R showed reduced forecast errors at most stations, whereas EXP_F exhibited increased forecast errors at approximately 20 out of 53 stations (Fig. S4).

Overall, WRF-Solar, particularly with the FARMS scheme, effectively provides accurate GHI forecasts at station-specific scales, with notable improvements under CLD and OVC. However, this result may be attributed to the fact that the FARMS shortwave radiation scheme accounts for cloud optical properties, which can lead to increased uncertainty under CLR.

3.1.3. *Diurnal variation analysis*

Since GHI exhibits substantial diurnal variations, analyzing its diurnal average pattern and assessing forecast errors in NWP models are essential. Under CLR, GHI follows a bell-shaped curve, rising rapidly after sunrise, peaking around noon, and gradually decreasing. In contrast, under CLD and OVC, fluctuations in clouds lead to irregular variations, increasing forecast uncertainty.

Fig. 9 shows the average diurnal variations of observations and experiments under the four sky conditions for the 1-day forecast during the summer season. The analysis for each sky condition is as follows: 1) For ALL, CNTL significantly overestimated GHI compared to EXP_R and EXP_F, with a peak difference of around 163 $W\ m^{-2}$ relative to observations. Although EXP_R reduced the overestimation compared to CNTL, it still exhibited a positive bias. Among all the experiments, EXP_F was the closest to observations, slightly overestimating GHI in the morning and underestimating it in the afternoon (Fig. 9a); 2) For CLR, CNTL consistently overestimated GHI throughout the day. EXP_R also exhibited an overestimation in the morning but closely aligned with observations in the afternoon. EXP_F overestimated GHI before 0200 UTC

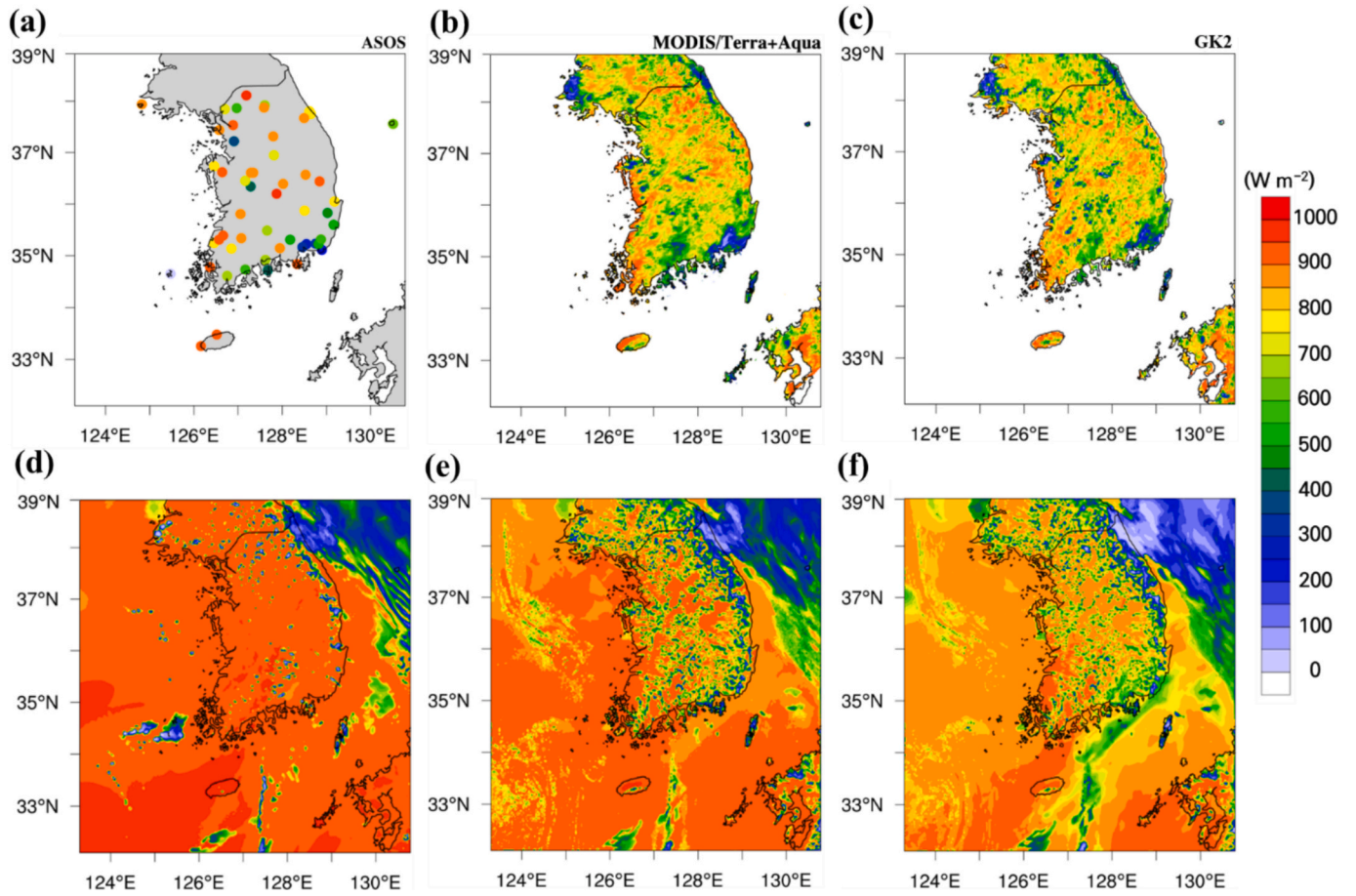


Fig. 14. Spatial distribution of GHI (color dots and shading; in $W\,m^{-2}$) at 0400 UTC on August 16, 2023, under clear sky conditions (CLR) across South Korea for observations and simulations: (a) ASOS (in-situ), (b) MODIS (satellite), (c) GK2A (satellite) (d) CNTL, (e) EXP_R, and (f) EXP_F.

(1100 LST) and underestimated it thereafter (Fig. 9b); 3) For CLD, all experiments showed greater overestimation in the morning than in the afternoon. Among them, EXP_F was the closest to observations, followed by EXP_R, while CNTL exhibited the largest overestimation, with a maximum deviation of approximately $282W\,m^{-2}$ (Fig. 9c); 4) For OVC, GHI was the lowest among the four sky conditions, with all experiments overestimating it, particularly around noon. EXP_F demonstrated the best agreement with observations, followed by EXP_R and CNTL (Fig. 9d).

In the 2-day forecast (Fig. S5), GHI exhibited slight differences from the 1-day forecast, but the variations among experiments and their diurnal patterns remained similar. Under CLR, EXP_F aligned most closely with observations until 0200 UTC (1100 KST), after which EXP_R showed better agreement. For other sky conditions, EXP_F demonstrated the best agreement with observations.

For CLR, EXP_F exhibited a relatively large underestimation, particularly in the afternoon. This can be attributed to the FARMS shortwave radiation scheme, which incorporates an improved representation of cloud optical properties, affecting the radiation calculations. While this scheme enhances forecast accuracy under conditions with high cloud variability, such as CLD and OVC, its cloud-related processes may have introduced unnecessary adjustments under CLR, where cloud effects are weak, leading to larger forecast errors.

3.1.4. *Regional analysis of diurnal GHI variability*

In South Korea, Jeollanam-do is the most active region for solar power generation [82]. This province benefits from vast plains and abundant solar radiation, supporting the steady expansion of large-scale solar power plants. As a result, Jeollanam-do has one of the highest installed solar capacities in the country [83]. Given its critical role in solar power generation, understanding the diurnal variability of GHI in Jeollanam-do is essential for optimizing solar energy production and ensuring a stable power supply. Since GHI directly affects PV output, analyzing its diurnal pattern is crucial for enhancing solar power forecasting and improving system efficiency. Moreover, the monsoon and non-monsoon periods exhibit significant seasonal differences. OVC prevails during the monsoon season, reducing solar radiation, whereas CLR dominates in the non-monsoon period, ensuring more stable solar energy production. To quantify these seasonal effects, we compared the diurnal variations of GHI between observations and experiments during these periods to evaluate seasonal differences.

Fig. 10 shows the classification of sky conditions based on K_t values for the monsoon season over South Korea, specifically from July 11 to 17, 2023. The classification includes three categories: CLR, CLD, and OVC. During this period, most regions across the country experienced OVC, followed by CLD, while CLR were observed only in limited areas.

Fig. 11 shows the diurnal variations of GHI from observations and all experiments at five sites in Jeollanam-do—(a) Gwangju, (b) Mokpo, (c) Boseong, (d) Yeosu, and (e) Gangjin—during the monsoon season from July 11 to 17, 2023. During the monsoon season, OVC generally persists, keeping GHI consistently low. However, intermittent cloud variations, which differ by location and time, can cause fluctuations in GHI. For example, at the Gwangju site on July 14 (Fig. 11a), GHI showed little variability and remained consistently low. In contrast, at the Boseong site on July 16 (Fig. 11c), GHI exhibited significantly great variability. Overall, GHI remained below the typical summertime peak.

Although the magnitude of errors varied by region, CNTL generally exhibited a significant overestimation of GHI, whereas EXP_R and EXP_F

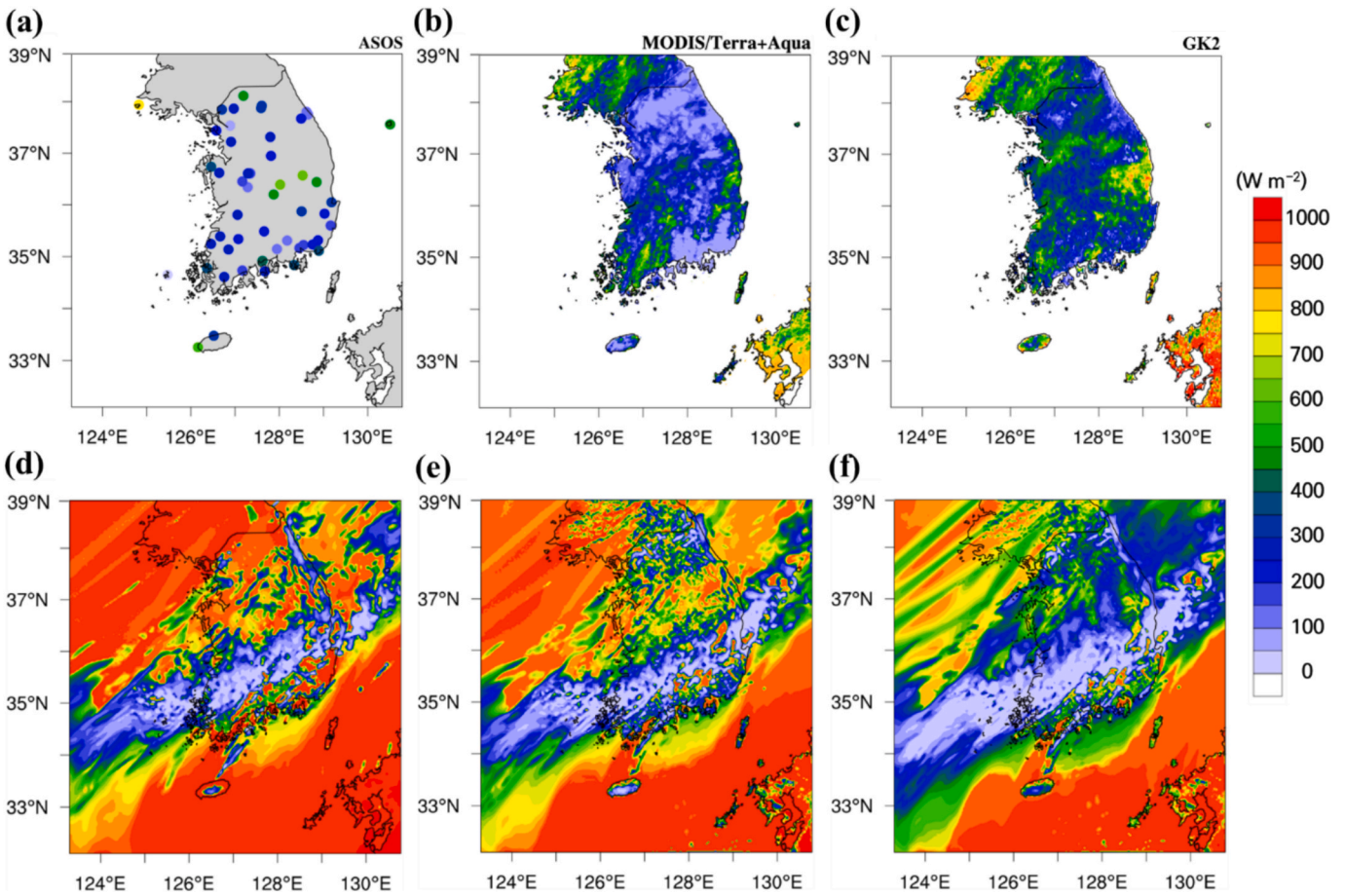


Fig. 15. Same as in Fig. 14, but at 0400 UTC on July 16, 2023, under cloudy (CLD) and overcast (OVC) sky conditions.

Table 6
Categorical verification metrics (POD_clr, POD_cld, FAR_clr, FAR_cld, HR, KSS, and MCF; in %) for evaluating the cloud detection performance of WRF and WRF-Solar, based on satellite (GK2A)-derived cloud detection data. Results are shown for both 1-day and 2-day forecasts.

		POD_clr	POD_cld	FAR_clr	FAR_cld	HR	KSS	MCF
1-day	WRF	75.0	81.7	30.5	14.6	79.3	56.7	18.3
	WRF-Solar	71.8	88.7	22.1	15.0	82.7	60.5	11.3
2-day	WRF	69.7	77.3	36.4	18.3	74.5	47.0	22.7
	WRF-Solar	66.9	85.0	28.2	18.2	78.4	51.9	15.0

produced more accurate results, with EXP_F showing the highest agreement with observations. This can be attributed to the inability of CNTL to adequately represent cloud properties and their radiative effects, whereas EXP_R and EXP_F incorporated the T-E microphysics and Deng shallow cumulus schemes, providing a more accurate representation of these factors. Furthermore, EXP_F improved forecast performance by incorporating the FARMS shortwave radiation scheme, which accounts for cloud optical properties.

However, in some locations, EXP_R and EXP_F tended to underestimate GHI. For instance, at the Gangjin site on July 15 and 16 (Fig. 11e), GHI was underestimated. This suggests that the experiments may have overestimated the impact of clouds on solar radiation. These findings emphasize the need for improving cloud–radiation-related parameterization to enhance GHI forecasts, particularly under CLD and OVC.

Fig. 12 shows the classification of sky conditions based on K_t values for a selected period within the non-monsoon season over South Korea, from July 29 to August 4, 2023. During this period, most regions across the country experienced almost entirely CLR.

Fig. 13 is the same as in Fig. 11 but for the period from July 29 to August 4, 2023. The observations indicate that persistent CLR produced a well-defined diurnal cycle of GHI, with overall higher solar radiation levels compared to the monsoon season. Under sustained CLR, all experiments closely followed the observed patterns. However, GHI variability increased at specific locations and times, such as Gwangju on August 3 and 4 (Fig. 13a) and Gangjin on August 4 (Fig. 13e), possibly due to cloud fluctuations. In these cases, CNTL failed to adequately capture this variability, whereas EXP_R and EXP_F exhibited similar trends, providing the most accurate representation of the observations.

3.2. Analysis of spatial distributions

General validation evaluates overall model performance, whereas case studies assess reliability for localized weather phenomena. Therefore, we analyzed the spatial distribution of GHI in specific cases to assess forecast accuracy.

We examined the spatial distributions of GHI for all experiments using in-situ data from ASOS and remote sensing observations from MODIS. MODIS data provide higher spatial resolution than ground-based observations, allowing for a more detailed representation of GHI distribution across the country. In contrast, in-situ data, which are

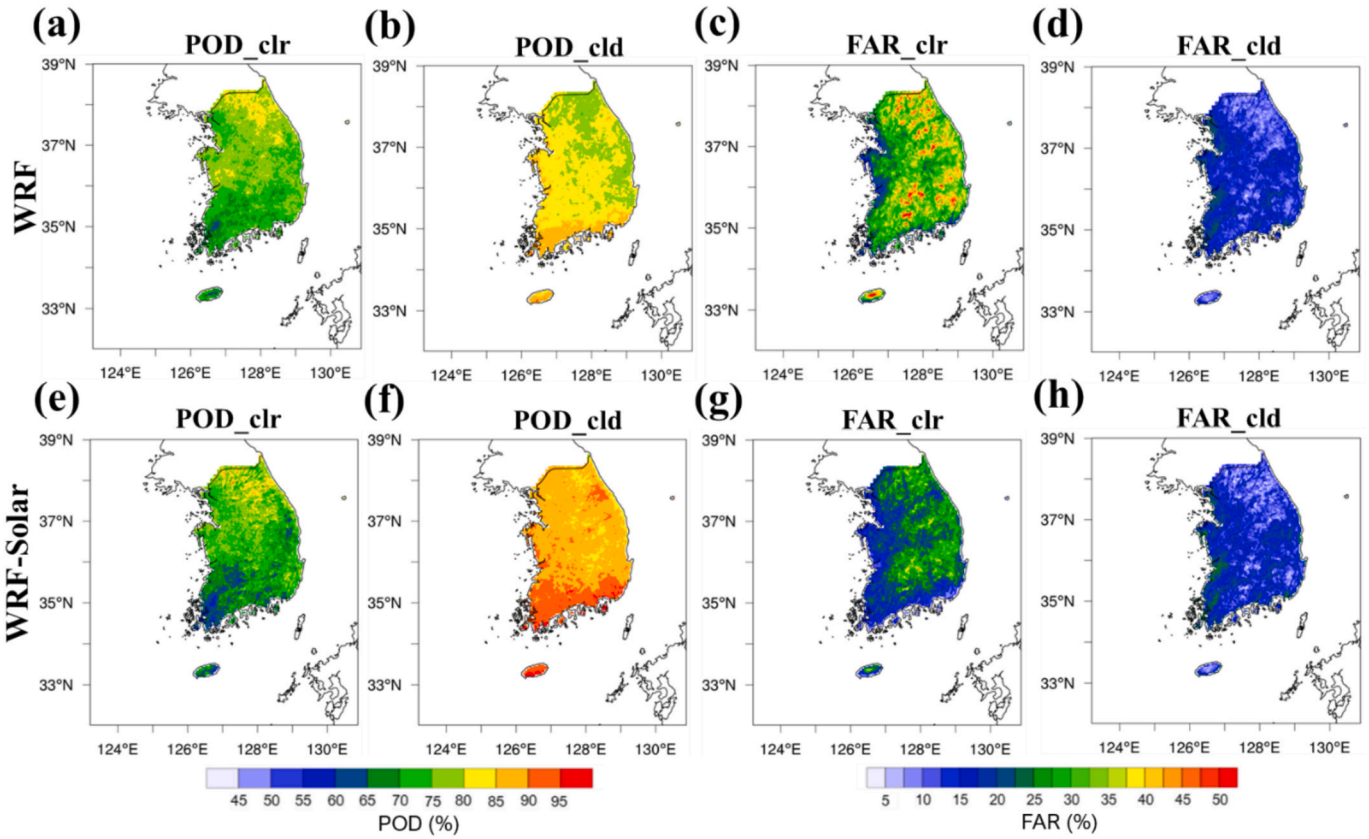


Fig. 16. Spatial distribution of categorical verification metrics for the 1-day forecasts during the summer of 2023. Top panels (a–d) show results from WRF, and bottom panels (e–h) show results from WRF-Solar. Each panel corresponds to the following verification metrics: (a) and (e) POD_clr (POD for clear-sky); (b) and (f) POD_cld (POD for cloudy-sky); (c) and (g) FAR_clr (false alarm rate for clear-sky); and (d) and (h) FAR_cld (false alarm rate for cloudy-sky).

directly measured in the environment, offer high accuracy and capture regional details. By analyzing both data sources, a more comprehensive and accurate assessment of the spatial distribution of GHI can be achieved.

The first case occurred on August 16, 2023, at 0400 UTC (1300 LST) under CLR nationwide (Fig. 14). The surface observations showed high GHI values exceeding 700 $W\,m^{-2}$ in the central and southern inland regions and Jeju Island, whereas lower values ranging from 200 to 650 $W\,m^{-2}$ were observed in the southern coastal areas (Fig. 14a). Although MODIS and GK2A showed some regional differences in GHI, both satellite-based datasets generally exhibit spatial patterns consistent with ASOS observations (Fig. 14b and 14c). The discrepancies between MODIS and GK2A can be attributed to differences in sensor characteristics, spatial and temporal resolutions, viewing geometry, cloud detection algorithms, and various processing differences inherent to each satellite system. The comparisons of the experiments with observations are as follows: 1) CNTL simulated high GHI values nationwide, exceeding *900 W m*$^{-2}$. In contrast, CNTL underestimated GHI along the Taebaek Mountain Range—extending from north to south along the east coast of South Korea, failing to capture regional variability (Fig. 14d); 2) EXP_R reduced overestimation observed in CNTL but still underestimated GHI along the Taebaek Mountain Range (Fig. 14e); 3) EXP_F simulated GHI most closely to the observations from ASOS, MODIS, and GK2A compared to CNTL and EXP_R, though underestimation persisted along the Taebaek Mountain Range. Overall, EXP_F demonstrated the best performance, most closely representing observed GHI (Fig. 14f).

The second case occurred on July 16, 2023, at 0400 UTC (1300 LST), during the monsoon season, with mostly OVC nationwide (Fig. 15). ASOS data showed GHI values below 300 $W\,m^{-2}$, whereas higher values ranging from 400 to 600 $W\,m^{-2}$ were observed in parts of the southeastern inland regions and western Jeju Island (Fig. 15a). Compared to ASOS observations, MODIS slightly underestimated GHI in parts of the central and southern regions, while overestimating it in the southwestern region (Fig. 15b). GK2A generally estimated higher GHI values than MODIS and showed better agreement with ASOS in regions where MODIS significantly underestimated GHI. However, it also showed a tendency to overestimate GHI in various areas (Fig. 15c). The differences between MODIS and GK2A were more pronounced under CLD and OVC conditions than under CLR. The comparison results are as follows: 1) CNTL significantly overestimated GHI in central and southern coastal regions and Jeju Island, with values exceeding 900 $W\,m^{-2}$, whereas it slightly underestimated GHI in some southern inland regions (Fig. 15d); 2) EXP_R reduced the overestimated GHI observed in CNTL but still showed higher values than the observations in central regions. Additionally, EXP_R continued to underestimate GHI in some southern inland regions (Fig. 15e); 3) EXP_F showed the best agreement with all observational datasets (ASOS, MODIS, and GK2A), reducing the overestimation in central regions found in CNTL and EXP_R. However, underestimation persisted in southern inland areas (Fig. 15f). Overall, EXP_F demonstrated the best performance under OVC, effectively reducing the overestimation observed in CNTL.

3.3. *Evaluation of cloud detection performance*

In this study, cloud detection data from the GK2A were used as the observational reference. To ensure reliability, data with low confidence levels were excluded from the analysis. Following the approach of Yang et al. (2022) [39], the known limitations of satellite-based cloud detection—particularly in identifying optically thin clouds—were not considered in this study.

In WRF-Solar, both EXP_R and EXP_F were configured to use the same cloud property inputs, allowing their GHI outputs to be compared

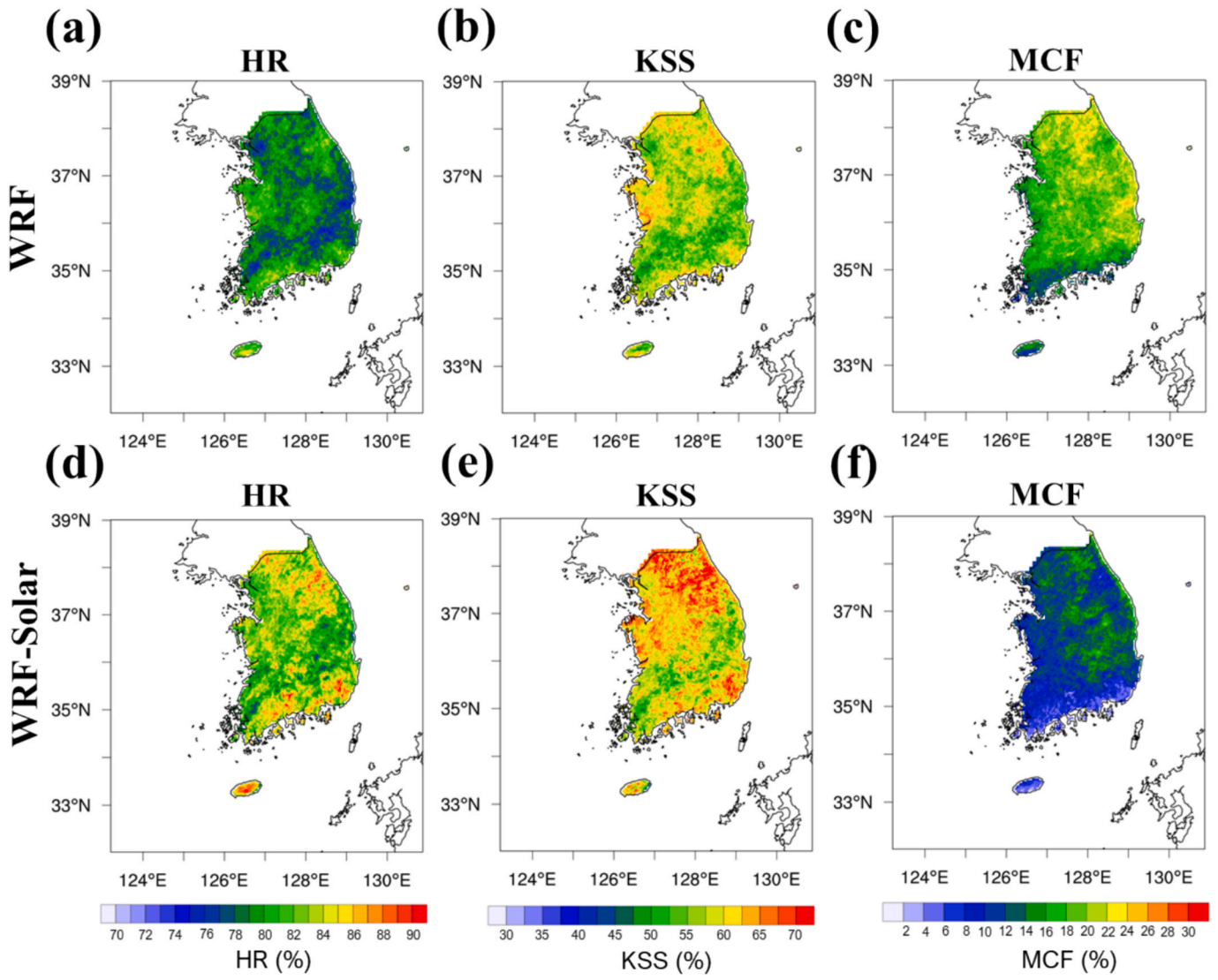


Fig. 17. Same as in Fig. 16, but for HR, KSS, and MCF for WRF (a–c) and WRF-Solar (d–f).

under consistent cloud conditions. This configuration provides consistent cloud inputs, making it possible to attribute differences in GHI forecasts between EXP_R and EXP_F primarily to the characteristics of their respective radiation schemes. Therefore, in this study, cloud detection performance was evaluated by comparing the results from WRF (CNTL) and WRF-Solar (EXP_R and EXP_F). Since EXP_R and EXP_F share the same cloud input fields, the cloud detection capability of WRF-Solar can be comprehensively assessed by analyzing both experiments together.

Table 6 summarizes the categorical metrics used to evaluate cloud detection performance based on GK2A-derived cloud data. For the 1-day forecasts, WRF exhibited slightly higher POD_clr (75.0 %) than WRF-Solar (71.8 %), indicating better detection of clear-sky occurrences. WRF-Solar, however, showed higher POD_cld and lower FAR_clr than WRF (88.7 % vs. 81.7 % and 22.1 % vs. 30.5 %, respectively), suggesting more accurate detection of cloudy-sky occurrences and fewer false alarms under clear-sky conditions. In contrast, WRF showed a slightly lower FAR_cld (14.6 % vs. 15.0 %) than WRF-Solar, indicating fewer false alarms under cloudy-sky conditions. These results indicate that WRF-Solar more accurately identified cloudy-sky occurrences and reduced false alarms for clear-sky occurrences. Although individual metrics such as POD and FAR offer useful insights, they may be misleading when the dataset is dominated by either clear- or cloudy-sky occurrences. Therefore, additional integrated metrics such as HR and KSS are essential for evaluating overall forecast performance based on sky condition. WRF-Solar achieved higher HR (82.7 %) and KSS (60.5 %), along with a lower MCF (11.3 %) compared to WRF, demonstrating improved agreement with GK2A-derived cloud occurrence data.

A similar pattern was observed for the 2-day forecasts. Although the overall performance slightly decreased compared to the 1-day forecasts, WRF-Solar consistently outperformed WRF across most metrics.

The improved categorical performance of WRF-Solar— as shown by higher POD_cld, HR, and KSS, and lower FAR_clr and MCF—indicates more accurate detection of sky conditions, especially under cloudy conditions. This enhanced identification of both clear- and cloudy-sky occurrences contributed to more reliable solar radiation forecasts by improving agreement with observed GHI.

Fig. 16 shows the spatial distributions of POD_clr, POD_cld, FAR_clr, and FAR_cld for 1-day during the summer of 2023. For clear-sky occurrences, WRF-Solar exhibited slightly lower POD_clr than WRF, particularly over the southwestern inland and eastern regions, indicating reduced capability in detecting clear-sky occurrences. However, FAR_clr were generally lower in WRF-Solar, suggesting fewer false alarms associated with clear-sky occurrences. In contrast, for cloudy-sky occurrences, WRF-Solar showed higher POD_cld across most regions, while exhibiting FAR_cld comparable to those of WRF, indicating

improved detection performance without an increase in false alarms.

Fig. 17 shows the spatial distributions of HR, KSS, and MCF for the 1-day forecasts. WRF-Solar outperformed WRF across most regions in all three metrics. HR were higher in WRF-Solar, indicating improved overall agreement with observed sky conditions. KSS also increased notably, reflecting enhanced discrimination between clear- and cloudy-sky occurrences. MCF values were substantially lower in WRF-Solar, highlighting fewer areas where the forecast failed to capture observed cloud presence.

Figs. S6 and S7 show the spatial distributions of categorical verification metrics for the 2-day forecasts. Despite the overall performance slightly decreased compared to the 1-day forecasts, WRF-Solar generally showed better agreement with GK2A across most metrics, including improved detection skill, reduced false alarms, and fewer misclassifications.

4. Conclusions

The increasing demand for renewable energy as a response to climate change has made solar power generation a crucial energy source. However, its efficiency and stability depend significantly on weather conditions, especially variations in global horizontal irradiance (GHI), which directly affects the reliability of photovoltaic (PV) power generation. Given these challenges, improving the accuracy of solar radiation forecasting is essential for optimizing energy production and ensuring grid stability.

To address this need, WRF-Solar was developed as the first numerical weather prediction (NWP) model specifically designed to enhance solar power forecasting [12]. Overseas, extensive research on WRF-Solar has been conducted; however, studies on its application in South Korea remain scarce. Therefore, this study is the first to evaluate the GHI forecasting performance of WRF-Solar in comparison with standard WRF in South Korea.

For this purpose, experiments were conducted using WRF (CNTL) and two WRF-Solar configurations (EXP_R and EXP_F). The key difference between the WRF-based experiment and the WRF-Solar experiments lies in the physical parameterization schemes, including specialized schemes in WRF-Solar—Thompson–Eidhammer (TE) microphysics, Deng shallow cumulus, and Fast All-sky Radiation Model for Solar applications (FARMS) shortwave radiation: Both EXP_R and EXP_F employed TE and Deng schemes, but they differed in their shortwave radiation schemes. EXP_R utilized the standard RRTMG scheme, whereas EXP_F adopted the FARMS scheme, which improves shortwave radiation representation by incorporating cloud optical properties.

The experiments were conducted during the summer of 2023, a period characterized by high and stable solar radiation but also significant variability due to the monsoon season. The forecast performance was evaluated by comparing simulations with GHI data from 53 observation stations and remote sensing data. The sky conditions were classified into four categories—all (ALL), clear (CLR), cloudy (CLD), and overcast (OVC). The forecast performance was assessed under each sky condition for both the first day (1-day) and the second day (2-day) forecasts. Distinguishing between 1-day and 2-day forecasts is crucial, as forecast uncertainty grows with lead time, leading to greater forecast errors and more complex power planning.

For MBE improvement rates over CNTL, EXP_F achieved more than 1.5 times the improvement of EXP_R across the four sky conditions, with the greatest improvement observed under CLR (EXP_R: 57.8 %, EXP_F: 95.3 %). For RMSE improvement rates over CNTL, EXP_R and EXP_F showed similar improvements under CLR (EXP_R: 7.2 %, EXP_F: 6.8 %), whereas EXP_F demonstrated greater improvements for ALL (EXP_R: 13.3 %, EXP_F: 19.6 %), CLD (EXP_R: 15.5 %, EXP_F: 23.2 %), and OVC (EXP_R: 19.9 %, EXP_F: 37.0 %). The spatial analysis results also indicated improvements in the experiments using WRF-Solar, with EXP_F exhibiting a greater overall performance improvement than EXP_R. In addition, WRF-Solar improved cloud detection performance across 1-day and 2-day forecasts, as indicated by categorical verification metrics.

The superior performance of WRF-Solar is attributed to the specialized physical parameterization schemes implemented in the model, including T-E microphysics, Deng shallow cumulus, and FARMS schemes. These enhancements led to significant improvements in forecast accuracy for GHI, particularly under cloudy conditions such as CLD and OVC.

Based on these findings, this study confirms that WRF-Solar effectively predicts GHI during the summer season in South Korea, demonstrating its potential to improve solar radiation forecasts. Given the direct relationship between GHI and PV power generation, the enhanced forecast accuracy of WRF-Solar has significant implications for optimizing PV power generation forecasting, ensuring grid stability, and facilitating the reliable integration of solar energy into the power system.

However, South Korea experiences four distinct seasons—spring, summer, fall, and winter— leading to seasonal variations in solar radiation characteristics, necessitating further research across different seasons. Additionally, the key parameters of physical parameterization schemes in numerical weather prediction (NWP) models are primarily derived from overseas observations and empirical values, which may not be fully compatible with climatic conditions and geographical features of South Korea. This limitation is especially noticeable when forecasting solar irradiance under cloudy-sky conditions, which are more difficult to predict than clear-sky conditions due to the high spatiotemporal variability of cloud cover and the complexity of cloud–radiation interactions. To improve forecast accuracy under these conditions, it is essential to optimize the physical parameters closely associated with these interactions. For this purpose, various observational datasets—such as ground-based measurements, satellite products, and reanalysis data—can be used to evaluate the performance of the model in simulating cloud properties and their radiative effects, providing a basis for parameter optimization.

Building on the findings of this study, future research should aim to optimize key WRF-Solar parameters related to solar radiation forecasting, with the goal of improving model applicability under the specific climatic and geographical conditions of South Korea. Such optimization is expected to enhance the accuracy and reliability of solar power generation forecasts, thereby supporting more stable and predictable energy planning.

CRediT authorship contribution statement

Ji Won Yoon: Writing – review & editing, Writing – original draft, Software, Methodology, Conceptualization. **Hyunsu Kim:** Methodology, Conceptualization. **Hae Soo Jung:** Validation, Software. **Seon Ki Park:** Writing – review & editing, Methodology, Conceptualization.

Declaration of competing interest

The authors declare that they have no known competing financial interests or personal relationships that could have appeared to influence the work reported in this paper.

Acknowledgement

This work was supported by the National Research Foundation of Korea (NRF) grant funded by the Korean government (MSIT) (2021R1A2C1095535) and partly by the Basic Science Research Program through the NRF, funded by the Ministry of Education (2018R1A6A1A08025520). S. K. Park was partly supported by the Specialized University Program for Confluence Analysis of Weather and Climate Data of the Korea Meteorological Institute (KMI), funded by the Korean government (KMA), and the Korea Power Exchange. The main calculations were performed using the supercomputing resources of the

KMA (National Center for Meteorological Supercomputer).

Appendix A. Supplementary data

Supplementary data to this article can be found online at https://doi.org/10.1016/j.ecmx.2025.101253.

Data availability

Data will be made available on request.

References

[1] Field, CB, Barros, VR (Eds.), 2014. Climate Change 2014 – Impacts, Adaptation and Vulnerability: Regional Aspects. Cambridge University Press, Cambridge.

[2] Raimi D, Zhu Y, Newell RG, Prest BC, Bergman A. Global Energy Outlook 2023: Sowing the Seeds of an Energy transition. Resources for the [accessed 27 February 2025] Future 2023. https://www.rff.org/publications/reports/global-energy-outlook-2023.

[3] Oh H, Hong I, Oh I. South Korea's 2050 carbon neutrality policy. East Asian Policy 2021;13(1):33–46. https://doi.org/10.1142/S1793930521000039.

[4] Kim JH, Kim SY, Yoo SH. Public acceptance of the "Renewable Energy 3020 Plan": evidence from a contingent valuation study in South Korea. Sustainability 2020;12(8):3151. https://doi.org/10.3390/su12083151.

[5] Wiatros-Motyka M, Fulghum N, Jones D. Global Electricity Review 2024. Ember; 2024. https://ember-energy.org/latest-insights/global-electricity-review-2024/ [accessed 27 February 2025].

[6] Gao XY, Huang CL, Zhang ZH, Chen QX, Zheng Y, Fu DS, et al. Global horizontal irradiance prediction model for multi-site fusion under different aerosol types. Renew Energy 2024;227:120565. https://doi.org/10.1016/j.renene.2024.120565.

[7] Li J, Ward JK, Tong J, Collins L, Platt G. Machine learning for solar irradiance forecasting of photovoltaic system. Renew Energy 2016;90:542–53. https://doi.org/10.1016/j.renene.2015.12.069.

[8] Sharma A, Kakkar A. Forecasting daily global solar irradiance generation using machine learning. Renew Sust Energ Rev 2018;82:2254–69. https://doi.org/10.1016/j.rser.2017.08.066.

[9] Solano A, Spínola J, Quispe A. Solar radiation forecasting using machine learning and ensemble feature selection. Energies 2022;15(19):7049. https://doi.org/10.3390/en15197049.

[10] Djeldjli H, Benatiallah D, Tanougast C, Benatiallah A. Solar radiation forecasting based on ANN, SVM and a novel hybrid FFA-ANN model: a case study of six cities south of Algeria. AIMS Energy 2024;12(1). https://doi.org/10.3934/energy.2024004.

[11] Liu J, Zang H, Ding T, Cheng L, Wei Z, Sun G. Harvesting spatiotemporal correlation from sky image sequence to improve ultra-short-term solar irradiance forecasting. Renew Energy 2023;209:619–31. https://doi.org/10.1016/j.renene.2023.03.122.

[12] Shan S, Ding Z, Zhang K, Wei H, Li C, Zhao Q. ACGL-TR: a deep learning model for spatio-temporal short-term irradiance forecast. Energ Conver Manage 2023;284:116970. https://doi.org/10.1016/j.enconman.2023.116970.

[13] Chen S, Li C, Stull R, Li M. Improved satellite-based intra-day solar forecasting with a chain of deep learning models. Energ Conver Manage 2024;313:118598. https://doi.org/10.1016/j.enconman.2024.118598.

[14] Gayathry V, Kaliyaperumal D, Salkuti SR. Seasonal solar irradiance forecasting using artificial intelligence techniques with uncertainty analysis. Sci Rep 2024;14(1):17945. https://doi.org/10.1038/s41598-024-68531-3.

[15] RajasundrapandiyanLeebanon T, Murugan NS, Kumaresan K, Jeyabose A. Long-term solar radiation forecasting in India using EMD, EEMD, and advanced machine learning algorithms. Environ Monit Assess 2025;197(310):1–36. https://doi.org/10.1007/s10661-025-13738-8.

[16] Bonavita M. On some limitations of current machine learning weather prediction models. Geophys Res Lett 2023;51(12):e2023GL107377. https://doi.org/10.1029/2023GL107377.

[17] Charlton-Perez AJ, Dacre HF, Driscoll S, Gray SL, Harvey B, Harvey NJ, et al. Do AI models produce better weather forecasts than physics-based models? a quantitative evaluation case study of storm Ciarán. npj Clim Atmos Sci 2024;7(1):93. https://doi.org/10.1038/s41612-024-00638-w.

[18] Olivetti L, Messori G. Advances and prospects of deep learning for medium-range extreme weather forecasting. Geosci Model Dev 2024;17(6):2347–58. https://doi.org/10.5194/gmd-17-2347-2024.

[19] Jimenez PA, Hacker JP, Dudhia J, Haupt SE, Ruiz-Arias JA, Gueymard CA, et al. WRF-Solar: Description and clear-sky assessment of an augmented NWP model for solar power prediction. Bull Am Meteorol Soc 2016;97(7):1249–64. https://doi.org/10.1175/BAMS-D-14-00279.1.

[20] Chaturvedi DK, Isha I. Solar power forecasting: a review. Int J Comput Appl 2016;145(6):28–50. https://doi.org/10.5120/ijca2016910728.

[21] El-Shahat D, Tolba A, Abouhawwash M, Abdel-Basset M. Machine learning and deep learning models based grid search cross validation for short-term solar irradiance forecasting. J Big Data 2024;11(1):134. https://doi.org/10.1186/s40537-024-00991-w.

[22] Ohtake H, Uno F, Oozeki T, Hayashi S, Ito J, Hashimoto A, et al. Solar irradiance forecasts by mesoscale numerical weather prediction models with different horizontal resolutions. Energies 2019;12(7):1374. https://doi.org/10.3390/en12071374.

[23] Skamarock WC, Klemp JB, Dudhia J, Gill DO, Barker DM, Duda MG, et al. A description of the Advanced Research WRF Version 3. NCAR Technical Note 2008. 2025,. doi:10.5065/D68S4MVH [accessed 27 February.

[24] Pielke RA, Cotton WR, Walko RL, Tremback CJ, Lyons WA, Grasso LD, et al. A comprehensive meteorological modeling system—RAMS. Meteorol Atmos Phys 1992;49:69–91. https://doi.org/10.1007/BF01025401.

[25] Baldauf M, Seifert A, Förstner J, Majewski D, Raschendorfer M, Reinhardt T. Operational convective-scale numerical weather prediction with the COSMO model: Description and sensitivities. Mon Weather Rev 2011;139(12):3887–905. https://doi.org/10.1175/MWR-D-10-05013.1.

[26] Kanamitsu M. Description of the NMC global data assimilation and forecast system. Weather Forecast 1989;4(3):335–42. https://doi.org/10.1175/1520-0434(1989)004<0335:DOTNGD>2.0.CO;2.

[27] Rogers E, DiMego G, Black T, Ek M, Ferrier B, Gayno G, et al. The NCEP North American mesoscale modeling system: Recent changes and future plans. Preprints, 23rd Conference on Weather Analysis and Forecasting/19th Conference on Numerical Weather Prediction, June 2009. https://ams.confex.com/ams/23WAF19NWP/techprogram/paper_154114.htm [accessed 27 February 2025].

[28] Jiménez PA, Alessandrini S, Haupt SE, Deng A, Kosovic B, Lee JA, et al. The role of unresolved clouds on short-range global horizontal irradiance predictability. Mon Weather Rev 2016;144(9):3099–107. https://doi.org/10.1175/MWR-D-16-0104.1.

[29] Haupt SE, Kosović B, Jensen T, Lazo JK, Lee JA, Jiménez PA, et al. Building the Sun4Cast system: Improvements in solar power forecasting. Bull Am Meteorol Soc 2018;99(1):121–36. https://doi.org/10.1175/BAMS-D-16-0221.1.

[30] Jiménez PA, Yang J, Kim JH, Sengupta M, Dudhia J. Assessing the WRF-Solar model performance using satellite-derived irradiance from the National Solar Radiation Database. J Appl Meteor Climatol 2022;61(2):129–42. https://doi.org/10.1175/JAMC-D-21-0090.1.

[31] Sawadogo W, Fersch B, Bliefernicht J, Meilinger S, Rummler T, Salack S, et al. Evaluation of the WRF-solar model for 72-hour ahead forecasts of global horizontal irradiance in West Africa: a case study for Ghana. Sol Energy 2024;271:112413. https://doi.org/10.1016/j.solener.2024.112413.

[32] Thaker J, Höller R. Evaluation of high resolution WRF solar. Energies 2023;16(8):3518. https://doi.org/10.3390/en16083518.

[33] Yue X, Tang X, Hu B, Chen K, Wu Q, Kong L, et al. Evaluation of the simulation performance of WRF-Solar for a summer month in China using ground observation network data. Atmos Oceanic Sci Lett 2024;100532. https://doi.org/10.1016/j.aosl.2024.100532.

[34] Khamees AS, Sayad T, Morsy M, Rahoma UA. Evaluation of three radiation schemes of the WRF-Solar model for global surface solar radiation forecast: a case study in Egypt. Adv Space Res 2024;73(6):2880–91. https://doi.org/10.1016/j.asr.2023.12.010.

[35] Choudhury D. Assessing aerosol effects on solar irradiance in the NEOM region with the WRF-solar model. Bull Atmos Sci Technol 2025;6(18):1–24. https://doi.org/10.1007/s42865-025-00105-1.

[36] Lee JA, Jiménez PA, Dudhia J, Saint-Drenan YM. Impacts of the aerosol representation in WRF-Solar clear-sky irradiance forecasts over CONUS. J Appl Meteorol Climatol 2023;62(2):227–50. https://doi.org/10.1175/JAMC-D-22-0059.1.

[37] Cheng X, Ye D, Shen Y, Li D, Feng J. Studies on the improvement of modelled solar radiation and the attenuation effect of aerosol using the WRF-Solar model with satellite-based AOD data over north China. Renew Energy 2022;196:358–65. https://doi.org/10.1016/j.renene.2022.06.141.

[38] Gentile S, Di Paola F, Cimini D, Gallucci D, Geraldi E, Larosa S, et al. 3D-Var data assimilation of SEVIRI radiances for the prediction of solar irradiance in Italy using WRF-Solar mesoscale model—preliminary results. Remote Sens 2020;12(6):920. https://doi.org/10.3390/rs12060920.

[39] Yang J, Sengupta M, Jiménez PA, Kim JH, Xie Y. Evaluating WRF-Solar EPS cloud mask forecast using the NSRDB. Sol Energy 2022;243:348–60. https://doi.org/10.1016/j.solener.2022.08.003.

[40] Kim JH, Munoz PAJ, Sengupta M, Yang J, Dudhia J, Alessandrini S, et al. The WRF-Solar ensemble prediction system to provide solar irradiance probabilistic forecasts. IEEE J Photovolt 2021;12(1):141–4. https://ieeexplore.ieee.org/document/9580552.

[41] Yang J, Kim JH, Jiménez PA, Sengupta M, Dudhia J, Xie Y, et al. An efficient method to identify uncertainties of WRF-Solar variables in forecasting solar irradiance using a tangent linear sensitivity analysis. Sol Energy 2021;220:509–22. https://doi.org/10.1016/j.solener.2021.03.044.

[42] Jung Y, Lee H, Kim J, Cho Y, Kim J, Lee YG. Spatio-temporal characteristics in the clearness index derived from global solar radiation observations in Korea. Atmos 2016;7(4):55. https://doi.org/10.3390/atmos7040055.

[43] Choi G, Lee DE. Changing human-sensible temperature in Korea under a warmer monsoon climate over the last 100 years. Int J Biometeorol 2020;64(5):729–38. https://doi.org/10.1007/s00484-020-01862-8.

[44] Lee BS, Kim SS. Climatological characteristics of the Changma season. J Korean Meteor Soc 1983;19:1–11.

[45] Ha KJ, Yun KS, Jhun JG, Park CK. Definition of onset/retreat and intensity of Changma during the boreal summer monsoon season. J Korean Meteor Soc 2005;41:927-42. https://www.kci.go.kr/kciportal/ci [accessed 27 February 2025] (in Korean with English abstract).

[46] Park JK, Das A, Park JH. A new approach to estimate the spatial distribution of solar radiation using topographic factor and sunshine duration in South Korea.

Energy Convers Manag 2015;101:30–9. https://doi.org/10.1016/j.enconman.2015.04.021.
[47] Skamarock WC, Klemp JB, Dudhia J, Gill DO, Barker DM, Duda MG, et al. A description of the Advanced Research WRF Version 3. NCAR Tech Note 2008;475(125):10–5065. https://doi.org/10.5065/D68S4MVH.
[48] Singh J, Singh N, Ojha N, Sharma A, Pozzer A, Kumar NK, et al. Effects of spatial resolution on WRF v3.8.1 simulated meteorology over the central Himalaya. Geosci Model Dev 2021;14(3):1427–43. https://doi.org/10.5194/gmd-14-1427-2021.
[49] Caldwell P, Chin HNS, Bader DC, Bala G. Evaluation of a WRF dynamical downscaling simulation over California. Clim Change 2009;95:499–521. https://doi.org/10.1007/s10584-009-9583-5.
[50] Mourre L, Condom T, Junquas C, Lebel T, Sicart JE, Figueroa R, et al. Spatio-temporal assessment of WRF, TRMM and in situ precipitation data in a tropical mountain environment (Cordillera Blanca, Peru). Hydrol Earth Syst Sci 2016;20(1):125–41. https://doi.org/10.5194/hess-20-125-2016.
[51] Dudhia J. WRF Physics Options NCAR WRF Basic Tutorial 2010;26:30. . https://citeseerx.ist.psu.edu/document [accessed 27 February 2025].
[52] Yoon JW, Lee E, Park SK. Improving the asian dust storm prediction using WRF-Chem through combinational optimization of physical parameterization schemes. Atmos Environ 2024;326:120461. https://doi.org/10.1016/j.atmosenv.2024.120461.
[53] Yoon JW, Lim S, Park SK. Combinational optimization of the WRF physical parameterization schemes to improve numerical sea breeze prediction using micro-genetic algorithm. Appl Sci 2021;11(23):11221. https://doi.org/10.3390/app112311221.
[54] Xie Y, Sengupta M, Dudhia J. A Fast All-sky Radiation Model for Solar applications (FARMS): Algorithm and performance evaluation. Sol Energy 2016;135:435–45. https://doi.org/10.1016/j.solener.2016.06.003.
[55] Thompson G, Eidhammer T. A study of aerosol impacts on clouds and precipitation development in a large winter cyclone. J Atmos Sci 2014;71(10):3636–58. https://doi.org/10.1175/JAS-D-13-0305.1.
[56] Ginoux P, Chin M, Tegen I, Prospero JM, Holben B, Dubovik O, et al. Sources and distributions of dust aerosols simulated with the GOCART model. J Geophys Res Atmos 2001;106(D17):20255–73. https://doi.org/10.1029/2000JD000053.
[57] Deng A, Seaman NL, Kain JS. A shallow-convection parameterization for mesoscale models. Part I: Submodel description and preliminary applications. J Atmos Sci 2003;60(1):34-56. doi:10.1175/1520-0469(2003)060<0034:ASCPFM>2.0.CO;2.
[58] Deng A, Gaudet B, Dudhia J, Alapaty K. Implementation and evaluation of a new shallow convection scheme in WRF. 26th Conf on Weather Analysis and Forecasting/22nd Conf on Numerical Weather Prediction, February 2–6, 2014, Atlanta, GA. Boston: Amer Meteor Soc. https://ams.confex.com/ams/94Annual/webprogram/Paper236925.html [accessed 27 February 2025].
[59] Ruiz-Arias JA, Dudhia J, Gueymard CA. A simple parameterization of the short-wave aerosol optical properties for surface direct and diffuse irradiances assessment in a numerical weather model. Geosci Model Dev 2014;7(3):1159–74. https://doi.org/10.5194/gmd-7-1159-2014.
[60] Pu Z, Kalnay E. Numerical weather prediction basics: Models, numerical methods, and data assimilation. In: Handbook of Hydrometeorological Ensemble Forecasting. Springer; 2019. p. 67–97.
[61] Slingo J, Palmer T. Uncertainty in weather and climate prediction. Philos Trans R Soc Math Phys Eng Sci 1956;2011(369):4751–67. https://doi.org/10.1098/rsta.2011.0161.
[62] Nakanishi M, Niino H. An improved Mellor–Yamada level-3 model: its numerical stability and application to a regional prediction of advection fog. Bound Layer Meteorol 2006;119:397–407. https://doi.org/10.1007/s10546-005-9030-8.
[63] Jiménez PA, Dudhia J, González-Rouco JF, Navarro J, Montávez JP, García-Bustamante E. A revised scheme for the WRF surface layer formulation. Mon Weather Rev 2012;140(3):898–918. https://doi.org/10.1175/MWR-D-11-00056.1.
[64] Ek MB, Mitchell KE, Lin Y, Rogers E, Grunmann P, Koren V, et al. Implementation of Noah land surface model advances in the National Centers for Environmental Prediction operational mesoscale Eta model. J Geophys Res Atmos 2003;108(D22). https://doi.org/10.1029/2002JD003296.
[65] Iacono MJ, Delamere JS, Mlawer EJ, Shephard MW, Clough SA, Collins WD. Radiative forcing by long-lived greenhouse gases: Calculations with the AER radiative transfer models. J Geophys Res Atmos 2008;113(D13). doi:10.1029/2008JD009944.
[66] Kain JS. The Kain–Fritsch convective parameterization: an update. J Appl Meteorol 2004;43(1):170–81. https://doi.org/10.1175/1520-0450(2004)043<0170:TKCPAU>2.0.CO;2.
[67] Prasad AA, Kay M. Assessment of simulated solar irradiance on days of high intermittency using WRF-solar. Energies 2020;13(2):385. https://doi.org/10.3390/en13020385.
[68] Guo Z, Fang J, Sun X, Yang Y. Sensitivity of summer precipitation simulation to microphysics parameterization over eastern China: Convection-permitting regional climate simulation. J Geophys Res Atmos 2019;124:9183–204. https://doi.org/10.1029/2019JD030295.
[69] Ineichen P, Perez R. A new airmass independent formulation for the Linke turbidity coefficient. Sol Energy 2002;73:151–7. https://doi.org/10.1016/S0038-092X(02)00045-2.
[70] Perez R, Ineichen P, Moore K, Kmiecik M, Chain C, George R, et al. A new operational model for satellite-derived irradiances: Description and validation. Sol Energy 2002;73:307–17. https://doi.org/10.1016/S0038-092X(02)00122-6.
[71] Lara-Fanego V, Ruiz-Arias JA, Pozo-Vázquez D, Santos-Alamillos FJ, Tovar-Pescador J. Evaluation of the WRF model solar irradiance forecasts in Andalusia (southern Spain). Sol Energy 2012;86(8):2200–17. https://doi.org/10.1016/j.solener.2011.02.014.
[72] Che Y, Chen L, Zheng J, Yuan L, Xiao F. A novel hybrid model of WRF and clearness index-based Kalman filter for day-ahead solar radiation forecasting. Appl Sci 2019;9(19):3967. https://doi.org/10.3390/app9193967.
[73] García-Rodríguez S, García I, García-Rodríguez A, Díez-Mediavilla M, Alonso-Tristán C. Solar ultraviolet irradiance characterization under all sky conditions in Burgos, Spain. Appl Sci 2022;12(20):10407. https://doi.org/10.3390/app122010407.
[74] Abdi EJ, Ali MM, Bilal B, Dia N, Ndongo M, Kebe CMF, et al. Seasonal analyses of solar radiation on flat ground for different state of sky: Case of Nouakchott. Mauritania Int J Phys Sci 2019;14(12):125–38.
[75] Sawadogo W, Bliefernicht J, Fersch B, Salack S, Guug S, Ogunjobi KO, et al. Global horizontal irradiance in West Africa: Evaluation of the WRF-Solar model in convection-permitting mode with ground measurements. J Appl Meteor Climatol 2023;62(7):835–51. https://doi.org/10.1175/JAMC-D-22-0186.1.
[76] Lee SH, Kim YH. Characteristics and error analysis of solar resources derived from COMS satellite. Atmos 2020;30(1):59–73. https://doi.org/10.14191/Atmos.2020.30.1.059 (in Korean with English abstract).
[77] Barnes WL, Xiong X, Guenther BW, Salomonson V. Development, characterization, and performance of the EOS MODIS sensors. Earth Observing Syst VIII 2003;5151:337–45. https://doi.org/10.1117/12.504818.
[78] Wang D. MODIS/Terra+Aqua Surface Radiation Daily/3-Hour L3 Global 1km SIN Grid V062 [Data set]. NASA EOSDIS Land Processes Distributed Active Archive Center; 2024. doi:10.5067/MODIS/MCD18A1.062.
[79] Ricchiazzi P, Yang S, Gautier C, Sowle D. SBDART: a research and teaching software tool for plane-parallel radiative transfer in the Earth's atmosphere. Bull Am Meteorol Soc 1998;79(10):2101–14. https://doi.org/10.1175/1520-0477(1998)079<2101:SARATS>2.0.CO;2.
[80] National Meteorological Satellite Center. Algorithm Theoretical Basis Document for GK2A/AMI Level 2 Shortwave Radiation. Korea Meteorological Administration; 2019 Oct 1. Available from: https://nmsc.kma.go.kr/resources/common/pdf/GK2A_SWRAD.pdf [Accessed 31 May 2025] (in Korean).
[81] National Meteorological Satellite Center. Algorithm Theoretical Basis Document for GK2A/AMI Level 2 Cloud Mask. Korea Meteorological Administration; 2019 Apr 15. Available from: https://nmsc.kma.go.kr/resources/common/GK2A_CLD.pdf [Accessed 31 May 2025] (in Korean).
[82] Park WY, Song YH, Abhyankar N, Moon HS, Paliwal U, Kim E, et al. A clean energy Korea by 2035: Transitioning to 80% carbon-free electricity generation. Cell Rep Sustain 2025;2(1):100262. https://doi.org/10.1016/j.crsus.2024.100262.
[83] Lee S. A Study on Energy Development and Policies in Jeollanam-do. Natl Public Law Rev 2023;19(1):37-74. doi:10.46751/nplak.2023.19.1.37 (in Korean with English abstract).